Special Section:
Insights into Subduction Zone Processes from Models and Observations of Exhumed Terranes

Key Points:

- The yield strength of the lithosphere was computed and compared with the upper-plate seismicity distribution of the southern Central Andes
- The brittle-ductile transition effectively bounds the depth extent of the seismogenic zone
- Seismicity localizes at the boundaries between weak and strong domains; slab steepening likely explains seismicity in the strong foreland

Supporting Information:

Supporting Information may be found in the online version of this article.

Correspondence to:

C. Rodriguez Piceda,
piceda@gfz-potsdam.de

Long-Term Lithospheric Strength and Upper-Plate Seismicity in the Southern Central Andes, 29°–39°S

C. Rodriguez Piceda[1,2] , **M. Scheck-Wenderoth[1,3]** , **M. Cacace[1]** , **J. Bott[1]** , and **M. R. Strecker[2]**

[1]HelmholtzZentrum GFZ – German Research Centre for Geosciences, Potsdam, Germany, [2]Institute of Geosciences, University of Potsdam, Potsdam, Germany, [3]RWTH Aachen University, Aachen, Germany

Abstract We examined the relationship between the mechanical strength of the lithosphere and the distribution of seismicity within the overriding continental plate of the southern Central Andes (SCA, 29°–39°S), where the oceanic Nazca Plate changes its subduction angle between 33°S and 35°S, from subhorizontal in the north (<5°) to steep in the south (∼30°). We computed the long-term lithospheric strength based on an existing 3D model describing variations in thickness, density, and temperature of the main geological units forming the lithosphere of the SCA and adjacent forearc and foreland regions. The comparison between our results and seismicity within the overriding plate (upper-plate seismicity) shows that most of the events occur within the modeled brittle domain of the lithosphere. The depth where the deformation mode switches from brittle frictional to thermally activated ductile creep provides a conservative lower bound to the seismogenic zone in the overriding plate of the study area. We also found that the majority of upper-plate earthquakes occurs within the realm of first-order contrasts in integrated strength (12.7–13.3 log Pam in the Andean orogen vs. 13.5–13.9 log Pam in the forearc and the foreland). Specific conditions characterize the mechanically strong northern foreland of the Andes, where seismicity is likely explained by the effects of slab steepening.

Plain Language Summary The southern Central Andes (29°–39°S) are one of the most seismically active regions along the South-American subduction zone. However, the causative dynamics behind localization of earthquakes in the South American plate are still not well understood. In this study, we computed the strength of the lithosphere (i.e., the resistance to deformation) with a specialized computer code and showcase that there exist a causative relationship with seismicity in the area. We found that earthquakes in the upper plate occur: (a) above the transition between domains with brittle to ductile deformation; and (b) where large and sharp horizontal strength contrasts exist. Specific conditions characterize the mechanically strong northern foreland of the Andes, where seismicity is likely explained by the additional effects of the oceanic subducted plate, where it transitions from a subhorizontal to a steep subduction angle. These results show the importance of quantifying the strength of the lithosphere and its spatial variations to better understand the distribution of seismicity records in the area.

1. Introduction

The ocean-continent convergent margin of the southern Central Andes (SCA, 29°–39°S), is characterized by an east-northeast-directed subduction of the oceanic Nazca Plate (NP) under the South American continental plate with a convergence rate of 6.1 cmyr^{-1} (Figure 1; Norabuena et al., 1999). A distinct geodynamic feature of the subduction margin is a change in subduction angle of the NP between 33°S and 35°S from the Chilean-Pampean flat-slab zone (<5° dip, 27°–33°S) to a steeper sector south of 35°S (∼30° dip; Figure 1). The SCA are one of the most seismically active regions along the South American convergent margin, where past seismic events had devastating impacts on humans, with loss of life and far-reaching economic repercussions (Alvarado & Beck, 2006; Alvarado, Barrientos, et al., 2009; Ammirati et al., 2019; Gregori & Christiansen, 2018; Ruiz & Madariaga, 2018). So far, seismological research in the SCA focused on understanding the causative dynamics of the recorded seismicity within the oceanic plate and along the subduction interface (e.g., Anderson et al., 2007; Cloos & Shreve, 1996; Hackney et al., 2006; Linkimer et al., 2020; Moreno et al., 2010, 2014; Wagner et al., 2020; Weiss et al., 2019), while less attention has been paid to the mechanisms controlling upper-plate seismicity (Alvarado et al., 2005; Alvarado, Barrientos, et al., 2009; Alvarado, Pardo, et al., 2009; Ammirati et al., 2019; Nacif et al., 2017; Smalley & Isacks, 1990; Smalley et al., 1993).
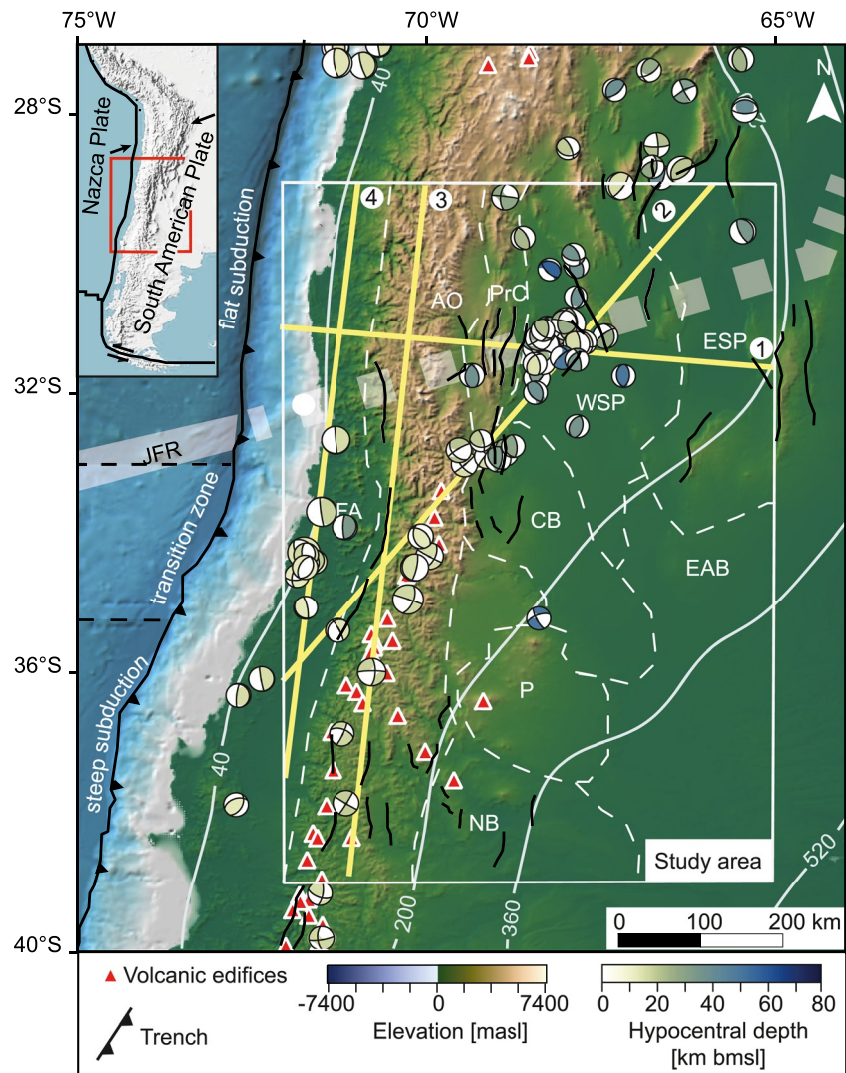
Figure 1. Topography and bathymetry of the southern Central Andes taken from the ETOPO1 global relief model (Amante & Eakins, 2009) overlain with focal mechanisms of upper-plate earthquakes from the Global Centroid Moment Tensor Catalog (Dziewonski et al., 1981; Ekström et al., 2012), color-coded by their hypocentral depth. Black dashed lines in the oceanic domain indicate the boundaries between subduction segments with steepening subduction angles from north to south. White lines are isodepth contours (km below mean sea level (bmsl)) of the top of the oceanic crust obtained from the Slab2 model (Hayes et al., 2018). The thick and dashed white lines show the offshore and projected tracks of the Juan Fernandez Ridge oceanic plateau, respectively (Yáñez et al., 2001). The white rectangle encloses the extent of the area modeled in this study. Thick black lines indicate the principal Quaternary tectonic faults (Sagripanti et al., 2017). The boundaries between the main morphotectonic provinces are shown by white dashed lines. The red triangles indicate active volcanoes. The yellow lines show the location of the profiles in Figures 5 and 6. Abbreviations of main tectonic provinces: AO = Andean orogen, CB = Cuyo Basin, ESP = Eastern Sierras Pampeanas, EAB = extra-Andean basins, FA = forearc, NB = Neuquén Basin, P = Payenia volcanic province, Prc = Precordillera, WSP = Western Sierras Pampeanas.

Previous studies on upper-plate earthquakes (e.g., SIEMBRA, ESP, CHARGE, CHARSME, and CHASE seismic experiments; Alvarado et al., 2005; Alvarado, Pardo, et al., 2009; Marot et al., 2014; Nacif et al., 2013, 2017; Olivar et al., 2018; Rivas et al., 2019; Venerdini et al., 2020) have depicted an heterogeneous earthquake distribution with seismic activity decreasing toward the south of the flat subduction segment, though such low seismicity rates could be partly attributed to a poorer coverage of seismic networks in the steep segment of the slab. A major outcome from these previous studies was to correlate monitored seismicity to localized weakening within neotectonic fault areas, either linked to Cenozoic structures or to compressional reactivation of inherited structures and fabrics (e.g., Astini et al., 1995; Azcuy & Caminos, 1987; Giambiagi et al., 2003; Jordan et al., 1983; Kay

et al., 2006; Llambias et al., 1993; Llambias & Sato, 1990; Mpodozis & Kay, 1990; Ramos, 1988). The analysis of focal-mechanism solutions of upper-plate seismicity in the SCA (Alvarado et al., 2010; Ammirati et al., 2019; global CMT catalog, Dziewonski et al., 1981; Ekström et al., 2012) shows a predominance of reverse and strike-slip faulting (Figure 1), indicating a preferential slip direction perpendicular and oblique to the plate-convergence direction, respectively (e.g., Farías et al., 2008; Tapia et al., 2015).

Despite these recent findings, the causative dynamics of the distributed upper-plate seismicity in the SCA where little to no record of present-day seismicity is found despite ubiquitous Quaternary faults is still subject of an open debate (e.g., Eastern Sierras Pampeanas, Neuquén Basin; Costa et al., 2000, 2020; Grimaldi & Dorobek, 2011; Martino, 2003; Sagripanti et al., 2017). This disparity between instrumentally recorded earthquakes and paleo-seismological manifestations in the Sierras Pampeanas is noteworthy and may result from long recurrence intervals. Alternatively, some authors proposed that variations in the long-term strength of the lithosphere may be responsible for the observed lack of seismicity in areas with pervasive active faulting, provided that the integrated strength of the plate exceeds the magnitude of plate-driving stresses (e.g., Liu & Zoback, 1997).

Whether a causative relationship exists between the long-term strength of the lithosphere and the spatial distribution of seismicity has been a long-standing matter of controversy (Burov, 2011; Chen et al., 2012; Chen & Molnar, 1983; Handy & Brun, 2004; Jackson et al., 2008; Scholz, 1988; Sibson, 1982). It has been proposed that the depth at which rocks transition from a preferentially brittle to a preferentially ductile mode of deformation (''brittle-ductile transition'' or BDT, Goetze & Evans, 1979) provides a conservative estimate of the down-dip extent of the seismogenic zone (e.g., Scholz, 1988; Sibson, 1982). Furthermore, compilations of crustal seismicity in different regions show that old or mafic crustal sectors are characterized by deep-seated seismicity, which supports the notion of a rheological control inherited from paleotectonic processes (e.g., Ammirati et al., 2013, 2016; Craig & Jackson, 2021; Jackson et al., 2008; Maggi et al., 2000; Pérez Luján et al., 2015).

In the SCA, a recently published 3D structural and thermal model (Rodriguez Piceda, Scheck Wenderoth, Gomez Dacal et al., 2021; Rodriguez Piceda, Scheck Wenderoth, Bott et al., 2021) provides the opportunity to quantify if such a spatial corelation exists between variations in long-term lithospheric strength and recorded active seismic deformation. In this study we derive the first 3D rheological model of the SCA, including available structural, compositional and thermal information of the area. Comparison of the results against the spatial distribution of upper-plate seismicity (International Seismological Centre, 2021) enables us to determine how variations in the long-term rheological configuration affect the localization of seismicity across the SCA, including the forearc and foreland regions.

1.1. Geologic Setting

The SCA encompass four main morphotectonic provinces: the forearc, the magmatic arc, the back-arc, and the foreland, each of them characterized by distinct structural and geomorphological features. The present-day configuration of the SCA is the result of a complex tectonic evolution that spans from the Neoproterozoic to the Quaternary, including episodes of terrane accretion, shortening, and extension (Astini et al., 1995; Azcuy & Caminos, 1987; Giambiagi et al., 2003; Jordan et al., 1983; Kay et al., 2006; Llambias & Sato, 1990; Mpodozis & Kay, 1990; Ramos, 1988). The ongoing subduction beneath the South American plate has been active since at least the Late Jurassic (Maloney et al., 2013 and references therein), although major pulses of Andean deformation are thought to have occurred during the Late Cretaceous and the Miocene (Boyce et al., 2020; Fennell et al., 2015). The onset of flat subduction north of 33°S is thought to have occurred at ~19 Ma (Jones et al., 2014, 2015, 2016), finally attaining its present-day subhorizontal angle at ~7–6 Ma (see Kay & Mpodozis, 2002; Kay et al., 2006; Ramos et al., 2002). The causative dynamics responsible for the tectonic evolution of the Central Andes is still disputed among the geoscientic community. Some authors argue that episodes of flat subduction are responsible for the migration of the deformation to the foreland (e.g., Oncken et al., 2006; Yáñez & Cembrano, 2004), while others link these compressional events to reactivation of inherited tectonic heterogeneities, such as crustal-scale sutures, independent of the role of the slab (Allmendinger et al., 1983; del Papa et al., 2013; Hongn et al., 2007; Hongn et al., 2010; Kley & Monaldi, 2002; Kley et al., 1999; Mon & Salfity, 1995; Ramos et al., 2002).

2. Methods

2.1. Modeling Approach

We computed the long-term yield strength of the lithosphere, that is, a proxy for the maximum differential stress that rocks are able to withstand without experiencing permanent deformation (Goetze & Evans, 1979) based on the approach described in Cacace and Scheck-Wenderoth (2016). In doing so, we assumed frictional behavior at shallow depths as described by Byerlee's law (Byerlee, 1968):

$$\Delta\sigma_b = f_f \rho_b g z \left(1 - f_p\right) \tag{1}$$

where $\Delta\sigma_b$ is the brittle yield strength, f_f is the Byerlee's friction coefficient (which depends on the internal friction coefficient μ_f and the faulting regime, see also Text S1 in Supporting Information S1), ρ_b is the bulk density, g is the gravitational acceleration, z the depth below topography and f_p is the pore fluid factor (defined as the ratio $\rho_f \rho_b^{-1}$, where ρ_f is the fluid density).

With increasing depths and temperatures, rocks tend to deform as a viscous (non-)Newtonian fluid, with dislocation creep being the dominant deformation mechanism in the lithosphere. In this study, we also included low-temperature plasticity (Peierls creep) at differential stresses greater than 200 MPa (Goetze et al., 1978; Katayama & Karato, 2008). The power laws describing dislocation creep (Equation 2) and low-temperature plasticity (Equation 3) can be expressed as:

$$\Delta\sigma_d = \left(\frac{\dot{\varepsilon}}{A_p}\right)^{\frac{1}{n}} \cdot \exp\left(\frac{H}{nRT}\right) \tag{2}$$

$$\Delta\sigma_D = \sigma_D \left(1 - \left[-\frac{RT}{Q_D} ln \frac{\dot{\varepsilon}}{A_D}\right]^{\frac{1}{2}}\right) \tag{3}$$

where $\Delta\sigma_d$ is the ductile yield strength, $\dot{\varepsilon}$ the reference strain rate, A_p the pre-exponential scaling factor for dislocation creep, n the power law exponent, H the creep activation enthalpy, T the temperature, R is the universal gas constant ($R = 8.314$ JK^{-1} mol^{-1}), σ_D the Peierls critical stress, Q_D the Dorn activation energy ($Q_D = 5.35e5$ Jmol^{-1}) and A_D the Dorn's law strain rate ($A_D = 5.7e11$ s^{-1}).

The yield strength ($\Delta\sigma_{max}$) at a given point is defined by the minimum of the brittle and ductile portions, $\Delta\sigma_b$ and $\Delta\sigma_d$ (Goetze & Evans, 1979). The depth at which the two curves intercept mark therefore the (BDT hereafter). In an attempt to better quantify the efficiency of viscous creep, we also discuss the results in terms of the effective viscosity (η_{eff}). This parameter is expressed by a power-law dependence of temperature and strain rate as (Burov, 2011):

$$\eta_{eff} = \frac{2^{\frac{1-n}{n}}}{3^{\frac{1+n}{2n}}} A^{-\frac{1}{n}} \dot{\varepsilon}^{\frac{1}{n}-1} \exp\left(\frac{H}{nRT}\right) \tag{4}$$

the material and temperature distributions used as input were derived from 3D lithospheric-scale models of the SCA (Rodriguez Piceda, Scheck Wenderoth, Gomez Dacal et al., 2021; Rodriguez Piceda, Scheck Wenderoth, Bott et al., 2021) and described in more detail in Section 2.1.1. The specific mechanical properties assigned to the lithospheric units of the model are subsequently outlined in Section 2.1.2.

2.1.1. 3D Structural and Thermal Models

The present-day geological configuration of the SCA in terms of layer geometries and densities has been derived based on a 3D lithospheric-scale model by Rodriguez Piceda, Scheck Wenderoth, Gomez Dacal et al. (2021). This model is a result of an data intensive integrative effort comprising different geological and geophysical data, including seismic tomography, reflection and refraction seismic profiles, sediment isopach maps and petrological data additionally constrained by gravity field modeling (see references in Rodriguez Piceda, Scheck Wenderoth, Gomez Dacal et al., 2021). The model covers a region extending along 1,100 km in the N-S direction, 700 km in the E-W direction (white rectangle in Figure 1) and 200 km in its depth extent. The layers composing the model were defined according to the main density contrasts in the lithosphere: (a) oceanic and continental sediments; (c) upper continental crystalline crust; (d) lower continental crystalline crust; (e) continental lithospheric mantle (6)
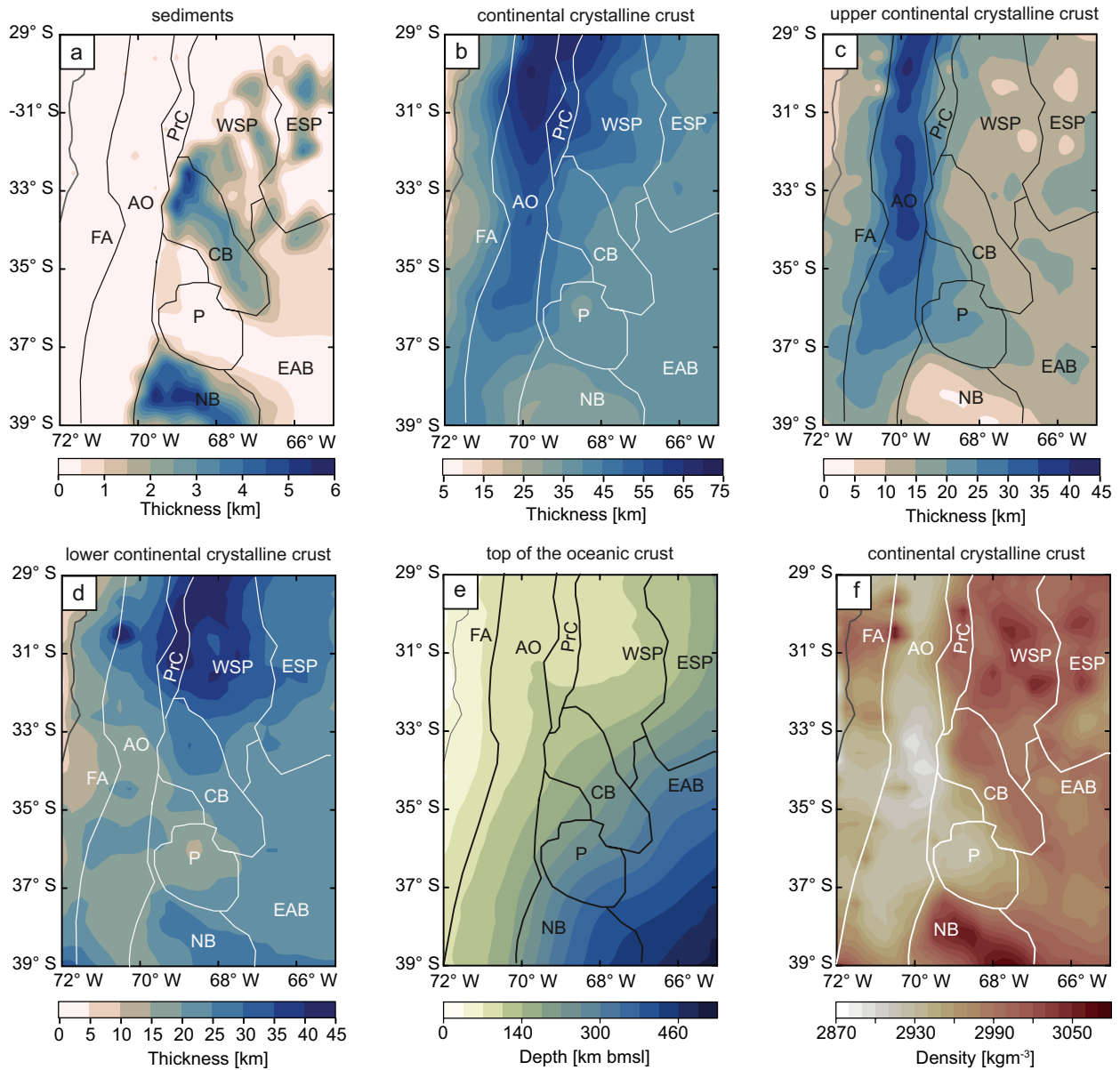
Figure 2. Main structural features of the southern Central Andes lithosphere from the model of Rodriguez Piceda, Scheck Wenderoth, Gomez Dacal et al. (2021): thickness of (a) sediments; (b) continental crystalline crust; (c) felsic upper continental crystalline crust; (d) mafic lower continental crystalline crust; (e) depth to the top of the oceanic crust derived from the Slab2 subduction zone geometry model (Hayes et al., 2018); (f) average density of the continental crystalline crust. Boundaries of the main morphotectonic provinces are overlain; for abbreviations see Figure 1.

shallow oceanic crust; (g) deep oceanic crust; (h) oceanic lithospheric mantle; and, (i) oceanic sub-lithospheric mantle. The main features of the model are depicted in Figure 2 in terms of the: (a) thickness of sediments; (b) thickness of continental crystalline crust; (c) thickness of upper continental crystalline crust; (d) depth to the top of the oceanic crust; and (d) average density of the continental crystalline crust.

The continental crystalline crust exhibits a first-order segmentation both in its thickness and density configuration, delineating three main crustal domains (Figure 2b): (a) the forearc, (b) the Andean orogen, and (c) the low-relief back-arc and foreland ("BAF", hereafter). The forearc is characterized by a normal continental crystalline crust (<35 km, Figure 2b) and intermediate to high average crustal densities (~2975 kg/m^3, Figure 2f). The Andean orogen has a thicker crystalline (~55 km, Figure 2b) and less dense (~2900 kg/m^3; Figure 2f) crust than its adjacent regions. The BAF can be segmented into three crustal sub-domains: (a) a thick, dense northern

domain (40–60 km, ~3,000–3,050 kg/m³); (b) a thin, high-density southern domain (~20 km, 40–60 km); and (c) a central domain with intermediate crustal thickness (35–45 km) and low to intermediate crustal densities (~2900–2950 kg/m³).

The temperature configuration used as input for the rheological calculations was derived from a thermal model of the SCA (Rodriguez Piceda, Scheck Wenderoth, Bott et al., 2021) covering the same region as the structural model. Crustal and mantle temperatures down to 50 km bmsl were computed assuming steady-state conductive conditions and using as input the structural model of Rodriguez Piceda, Scheck Wenderoth, Gomez Dacal et al. (2021). Thermal properties were assigned to each layer of the model according to its prevailing lithology and in order to best fit available wellbore temperature measurements (Collo et al., 2018). The average surface temperature distribution (Copernicus Climate Change Service (C3S) (2019)) was assigned as upper thermal boundary condition. The temperature distribution at 50 km depth, lower thermal boundary condition, was estimated from conversion of a S-wave tomography (Assumpção et al., 2013) following Goes et al. (2000). In a similar fashion, also the thermal field between 50 and 200 km bmsl has been derived from a direct conversion of the seismic tomography. More details on the thermal modeling approach can be found in the Text S2 in Supporting Information S1.

Figure 5.3 shows the depth maps for the 450°C and 650°C isotherms, as they are thought to correspond to major rheological contrasts at crustal and uppermost mantle levels. Additional depth slices are included in the Supporting Information S2 (Figure S1 in Supporting Information S1). The 450°C isotherm shallows in the model domains of thickened upper crust enriched with radiogenic minerals (orogen), resulting in warmer temperatures (Figure 5.3a). Conversely, it deepens in the crustal domains characterized by a thin upper crust, a thick mafic lower crust and where the slab is at relatively shallow depth and, therefore, is colder than where the subduction angle is steeper (forearc and BAF). As a result, 450°C the isotherm is located within the upper crust of the orogen; within the lower crust in the BAF; and within the continental lithospheric mantle in the forearc. The 650°C isotherm exhibits a similar pattern as the 450°C isotherm (Figure 5.3b), shallowing in the Andean orogen and deepening in the forearc and the northern BAF. It is located mostly within the lower crust in the orogen and northernmost BAF; in the continental mantle in the remaining BAF and eastern forearc, and within the slab in the western forearc. Relative differences in the overall pattern of the two isotherms are limited to the fact that the 450°C isotherm mirrors the thickness of the upper crust (Figure 5.2b) whereas the 650°C isotherm follows the topology of the top of the oceanic crust (''subduction interface'' hereafter; Figure 5.2e).

2.1.2. Rheological Properties

We assigned constant rheological properties for each layer according to its prevailing lithology. These values were taken from studies based on experimental rock mechanics (Table 1 (Afonso & Ranalli, 2004; Gleason & Tullis, 1995; Goetze & Evans, 1979; Hirth & Kohlstedt, 1996; Ranalli & Murphy, 1987; Wilks & Carter, 1990))., from the layers densities - the latter constrained by gravity modeling (Rodriguez Piceda, Scheck-Wenderoth, Gomez Dacal, et al., 2021) and seismic velocities (Araneda et al., 2003; Contreras-Reyes et al., 2008; Marot et al., 2014; Pesicek et al., 2012; Scarfì & Barberi, 2019). Since material properties for similar lithologies can differ between different laboratory-based studies, we selected creep parameters in a way to ensure that felsic layers are weaker than mafic layers. A detailed description of how we selected all properties is provided in the Text S3 in Supporting Information S1.

An important role in the accommodation of deformation is taken by the subduction interface (Sobolev et al., 2006), which in our model is underlain by an oceanic crustal body (~7 km average thickness). The uppermost part of this body (~3 km thickness) is interpreted as being made up of a mélange of metasediments, serpentinites and serpentinized peridotites, based on exhumed rock assemblages at surface and related to the subduction channel (e.g., Vannucchi et al., 2008). Therefore, to model its mechanical behavior, we assigned a ''weak quartzite'' rheology (Wilks & Carter, 1990), consistent with a tectonic mélange.

The Byerlee's friction coefficient f_f of all considered layers (except for the subduction interface) was set to 2 (equivalent to a nominal internal friction coefficient μ_f of 0.65) to reflect the overall compressive regime at the convergent margin. The pore-fluid factor of these layers was set to 0.36, indicative of near hydrostatic conditions. For the subduction interface, in order to represent the mélange at the subduction channel, we imposed different values for both the Byerlee's friction coefficient and the pore-fluid factor of the uppermost oceanic crustal body, being equal to 0.03 and 0, respectively. These values are consistent with an internal friction coefficient μ_f of

Table 1
Rheological Properties of the Model Units

Model layer	Prevailing lithology	Type rheology	Dislocation creep parameters			Frictional parameters		
			Activation enthalpy H (Jmol^{-1})	n	Pre-exponential factor (Pa^{-n} s^{-1})	Pore-fluid factor f_f	Byerlee's friction coefficient f_f	Bulk Density (kgm^{-3})[g]
Oceanic/Continental sediments	Siliciclastic	Wet granite[a]	1.37e + 05	1.9	7.94e−16	0.36	2	2,300/2,400
Upper crust	Diorite	Dry quartz diorite[a]	2.19e + 05	2.4	5.02e−18	0.36	2	2,800
Lower crust	Mafic granulite	Dry mafic granulite[b]	4.45e + 05	4.2	8.83e−22	0.36	2	3,100
Continental lithospheric mantle/ oceanic sub-lithospheric mantle	Moderately depleted lherzolite	Dry Olivine[c]	5.10e + 05	3	7.00e−14	0.36	2	3,340
Shallow oceanic crust (weak)	Mélange (serpentinites, serpentinized peridotites, metasediments)	Wet quartzite[d]	2.23e + 05	4	1.00e−28	0	0.03	2,900
Shallow oceanic crust (strong)	Basalt	Dry diabase[e]	4.85e + 05	4.7	5.05e−28	0.36	2	2,900
Deep oceanic crust	Eclogite	Dry diabase[e]	4.85e + 05	4.7	5.05e−28	0.36	2	3,200
Oceanic lithospheric mantle	Harzburgite	Dry peridotite[f]	5.35e + 05	3.5	5.01e−17	0.36	2	3,360

[a]Ranalli and Murphy (1987). [b]Wilks and Carter (1990). [c]Goetze and Evans (1979). [d]Gleason and Tullis (1995), quartzite weakened by increasing pre-exponential factor A by 10 times (Sobolev & Babeyko, 2005). [e]Afonso and Ranalli (2004). [f]Hirth and Kohlstedt (1996). [g]Rodriguez Piceda, Scheck Wenderoth, Gomez Dacal et al. (2021); Rodriguez Piceda, Scheck Wenderoth, Bott et al. (2021).

0.015, which is considered appropriate to describe the frictional behavior of the subduction channel at the latitude of the SCA (Sobolev et al., 2006).

For all modeled layers (except for the subduction interface), the strain rate $\dot{\epsilon}$ was set to 6.5e−16 s^{-1}, which is consistent with the amount of shortening produced in the SCA in the last 18 Ma (Giambiagi et al., 2012) and with GNSS measurements (Drewes & Sánchez, 2017; Text S4 in Supporting Information S1). This latter assumption might be too restrictive for convergent margins, where strain-rate values can be non-uniform (e.g., Kreemer et al., 2014). We further discuss the sensitivity of the results to variations in strain rate values in Section 4.1. The subduction interface, as a plate boundary, is subjected to strain rates up to four orders of magnitude higher than the continental and oceanic plates, as shown by petrological evidence derived from rocks exhumed from the subduction channel (Platt et al., 2018) and results from geodynamic numerical modeling of subduction zones (Muldashev, 2017). In an attempt to model this behavior, we set an $\dot{\epsilon}$ of 1e−12 s^{-1} for the uppermost sectors of the oceanic crustal body.

2.2. Seismic Catalogue Data

Computed lithospheric strengths (and associated effective viscosities) were compared against the distribution of seismic events as based on the reviewed bulletin of the International Seismological Centre covering a period from 1995 to 2018 (International Seismological Centre, 2021). Our choice stems from: (a) the size of the catalog comprising approximately 44,100 unfiltered events, (b) the fact that events have been manually reviewed by ISC analysts, and (c) the integration of hypocentral depth-errors. Although the catalog completeness may vary in both space and time, we prioritized the earthquake hypocenter location over their magnitude of completeness, in line with our main research goal, this is, to relate modeled lithospheric strength variations with the spatial distribution of seismicity. In order to maximize the reliability of the investigation, all events with fixed depths or associated with an error >5 km were removed from the data set. To carry out our comparative study, we also separated all upper-plate events based on their location with respect to the depth of the top oceanic crust from the subduction zone geometry model Slab2 (Hayes et al., 2018) as their lower boundary. Our choice of this surface to represent the subduction interface stems from the consistency between fault-strike orientations inferred from the Slab2 model and GCMT focal mechanisms solutions (Chen et al., 2020). Since the Slab2 model has an uncertainty of
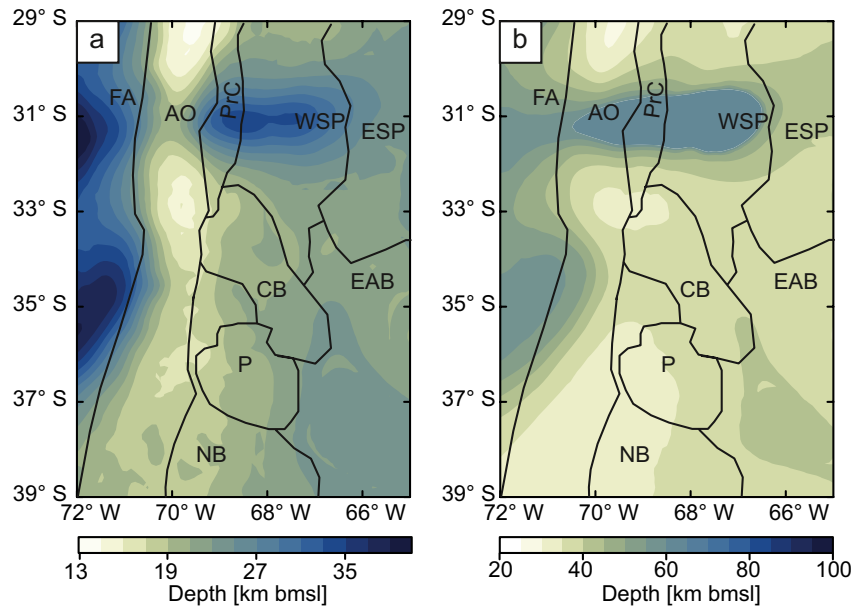
Figure 3. Depth of the (a) 450°C and (b) 650°C isotherms across the modeled area according to the lithospheric-scale model of Rodriguez Piceda, Scheck Wenderoth, Gomez Dacal et al., 2021; Rodriguez Piceda, Scheck Wenderoth, Bott et al., 2021). Boundaries of the main morphotectonic provinces are also marked with black lines; for abbreviations see Figure 5.1.

up to tens of kilometers (Text S5 in Supporting Information S1), we defined as maximum depth of upper-plate seismicity the depth of the top oceanic crust plus the uncertainty of the Slab2 model. After filtering the data, 2,174 events with moment magnitude (Mw) between 1 and 7.2 were available for our final comparison against the rheological model.

Figure 4 shows maps of event density and the seismogenic depth D95 (depth above which 95% of events occur) for the upper-plate seismicity. In the forearc and in the central part of the orogen, seismic events preferentially nucleate at depths <30 km bmsl. In the BAF regions of the Precordillera, the Sierras Pampeanas, and the Cuyo basin, that is, generally above the flat-slab segment, seismicity occurs at deeper crustal levels (D95 = ~40 km, Figures 4a-4b), whereas the southern and northern parts of the orogen and the remaining foreland regions are mostly aseismic.

3. Results

Figure 5 depicts the integrated strength of (a) the continental crust (IS_c) and (b) the whole lithosphere (IS_L) for the study area. Both maps exhibit a heterogeneous strength distribution, with mechanically strong domains in the forearc and the northern BAF along the flat-slab segment (IS_C = 13.3–13.6 log Pa m; IS_L = 13.5–13.9 log Pa m) and a mechanically weaker domain within the orogen proper (IS_C = 12.7–13 log Pa m; IS_L = 12.7–13.3 log Pa m). The orogen is characterized by a local increase in both crustal and total lithospheric strength at approximately 31°S and between 33°S and 35°S. A change in the observed overall positive correlation between IS_C and IS_L is found within the offshore part of the forearc, which displays a weak crust (IS_C < = 12.2 log Pa m) underlain by a strong mantle (IS_L > =13.6 log Pa m).

Modeled variations in both IS_C and IS_L correlate with the temperature distribution as represented by the isotherms shown in Figure 3. Mechanically stronger domains in the forearc and the northern foreland correspond to colder domains, and the weak orogenic domain is characterized by steeper geothermal gradients. We also found a spatial correlation between the thickness distribution of the radiogenic upper continental crystalline crust (Figure 2c) and the IS_L distribution. Crustal domains with a thicker upper continental crystalline crust (orogen) correlate with lower lithospheric strength values, whereas a thin upper continental crystalline crust is characterized by an increase in lithospheric strength (forearc and northern foreland). This negative correlation between the thickness of the upper continental crust and lithospheric strength stems from the role of this layer with respect to the whole
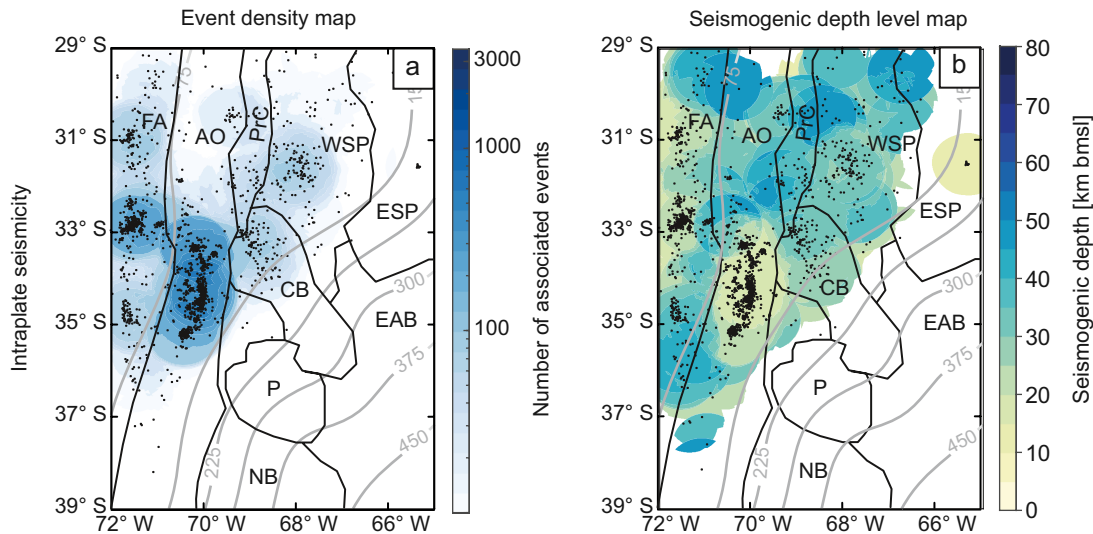
Figure 4. Spatial distribution of event density and of seismogenic depth D95 (depth above which 95% of events occur) derived by considering a circular bin of 75 km radius (logarithmic scale) for upper-plate seismicity. Single seismic events are marked with black dots. Isodepth contours of the top of the oceanic slab (Hayes et al., 2018) are shown as gray lines. Boundaries of the main morphotectonic provinces are also marked with black lines; for abbreviations see Figure 5.1.

thermal budget of the plate, due to its dominant felsic lithology and high radiogenic potential. A pronounced upper crustal thickness translates into higher temperatures and, therefore, lower values of lithospheric strength. In contrast, the lower crust is comparatively depleted in heat-producing elements (Vilà et al., 2010), thus in regions with a thick lower crust (northern foreland) the thermal input decreases, which results in lower temperatures and, therefore, higher values of lithospheric strength.

In an attempt to evaluate the contribution of the different layers (crust and lithospheric mantle) to the make-up of the integrated strength of the plate we present in Figure 5c a map showing the distribution of their strength ratio. The strength ratio can be used as a proxy of the dominance of the crustal component over the lithospheric strength. Accordingly, a ratio close to 100% means that the crust is the only contributor to lithospheric strength, whereas a ratio close to 0% means that the lithospheric strength resides almost entirely in the mantle. The forearc and the Sierras Pampeanas exhibit a low ratio (25%–40%), which indicates that the mantle is the stress-bearing domain of the plate. The remaining areas are instead characterized by higher strength ratios, with maximum values along the orogen and northernmost BAF (north of 30°S), thereby exhibiting a higher crustal contribution to the overall lithospheric strength.

To gain further insight into the rheological configuration of the area, we computed in Figure 5d the mechanical thickness (H_L). H_L is an effective parameter quantifying the load-bearing thickness of the whole plate and it is defined as the integrated thickness having a strength above a critical threshold, usually set at 10 MPa (Ranalli, 1994). Below this threshold, the strength of the plate becomes insignificant; thus, dissipation of elastic energy in these domains should be considered negligible. Therefore, H_L can be used to estimate the coupling-decoupling conditions in the crust and mantle of the continental plate (e.g., Tesauro et al., 2012). If H_L is greater than the thickness of the continental crust, then these two layers are mechanically coupled. Conversely, if H_L is smaller than the thickness of the continental crust, then these two layers are mechanically decoupled. Given these characteristics, H_L provides a more appropriate quantitative metric for direct comparison with the map showing seismogenic depth than other rheological parameters, such as elastic thickness Te. This is because visco-plastic models usually predict lower stresses in regions of high strain than purely elastic models (Anikiev et al., 2020; Ranalli, 1994).

Figure 5d illustrates the spatial variations in H_L together with the coupling-decoupling conditions within the continental crust and mantle. H_L displays a positive correlation with the IS_L map (Figure 5b), with greater values in the orogen at ~32°S, the Sierras Pampeanas, the Precordillera, and the forearc (H_L = 60–135 km). These values contrast with the reduced mechanical thickness of the orogen (H_L < 60 km), with the exception of the orogenic sector at 32°S (H_L = 60–90 km). From these results, we can conclude that the continental crust and mantle are
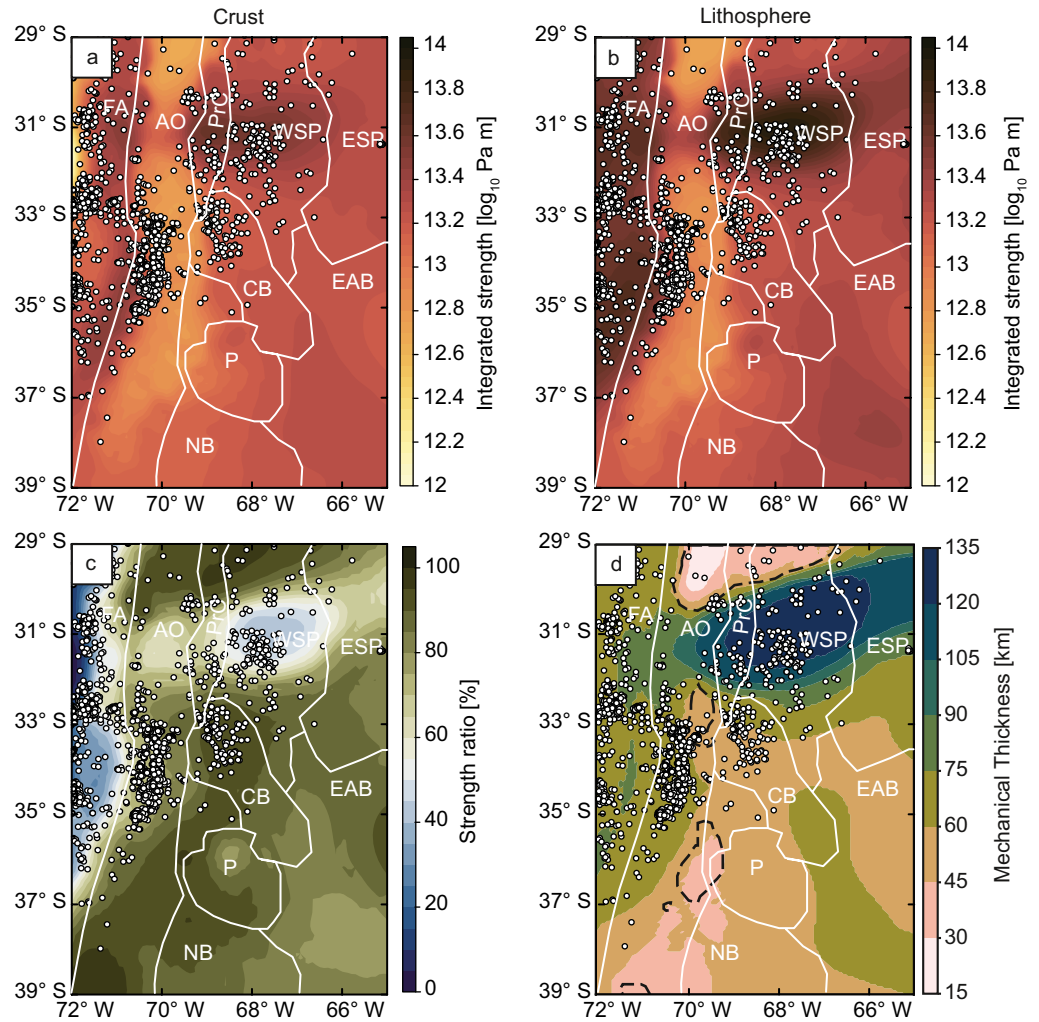
Figure 5. Integrated strength of (a) continental crust and (b) lithosphere; (c) strength ratio between integrated strength of the crust and of the lithosphere (strength ratio = IS_C/IS_L * 100) (d) mechanical thickness (i.e., thickness of the plate having a strength above a critical threshold of 10 MPa); with model domains where the crust and mantle of the continental plate are mechanically decoupled marked by enclosing black dashed lines. Upper-plate seismicity is represented by white circles. Boundaries of the main morphotectonic provinces are also marked with white lines; for abbreviations see Figure 1.

mechanically decoupled, mainly along the orogenic axis. The modeled mechanical thickness shows a similar spatial distribution as the one of the seismogenic base obtained independently from the seismic catalogue: deeper upper-plate seismicity (D95 = 40–50 km) occurs where the mechanical thickness is >100 km within the northern BAF regions. In contrast, shallow upper-plate events (D95 < 30 km) takes place where the mechanical thickness is 60–75 km within the forearc and in the central part of the orogen.

Within the continental plate, the distribution of the mechanical strength and effective viscosity also varies quite significantly with depth, as can be seen from the profiles that traverse our 3D model shown in Figure 6 (see also Figure S5 in Supporting Information S1). The location of these profiles was chosen according to the regions displaying the largest amount of seismic events: Profile 1 crosses the region from East to West across the flat-slab segment; Profile two is oriented NE to SW; Profile 3 traverses the region along the orogen; and Profile 4 is located along the forearc (Figure 1).

In the forearc, strength increases up to 1.5 GPa at mantle depths of 50 km (Figure 6, Profiles 1–2 and 4). This corresponds to an effective viscosity between 24 and 25 log Pa s (Figure S5 in Supporting Information S1). In the orogen the highest strength values (0.6 GPa), and corresponding effective viscosity (24 log Pa s), are reached at
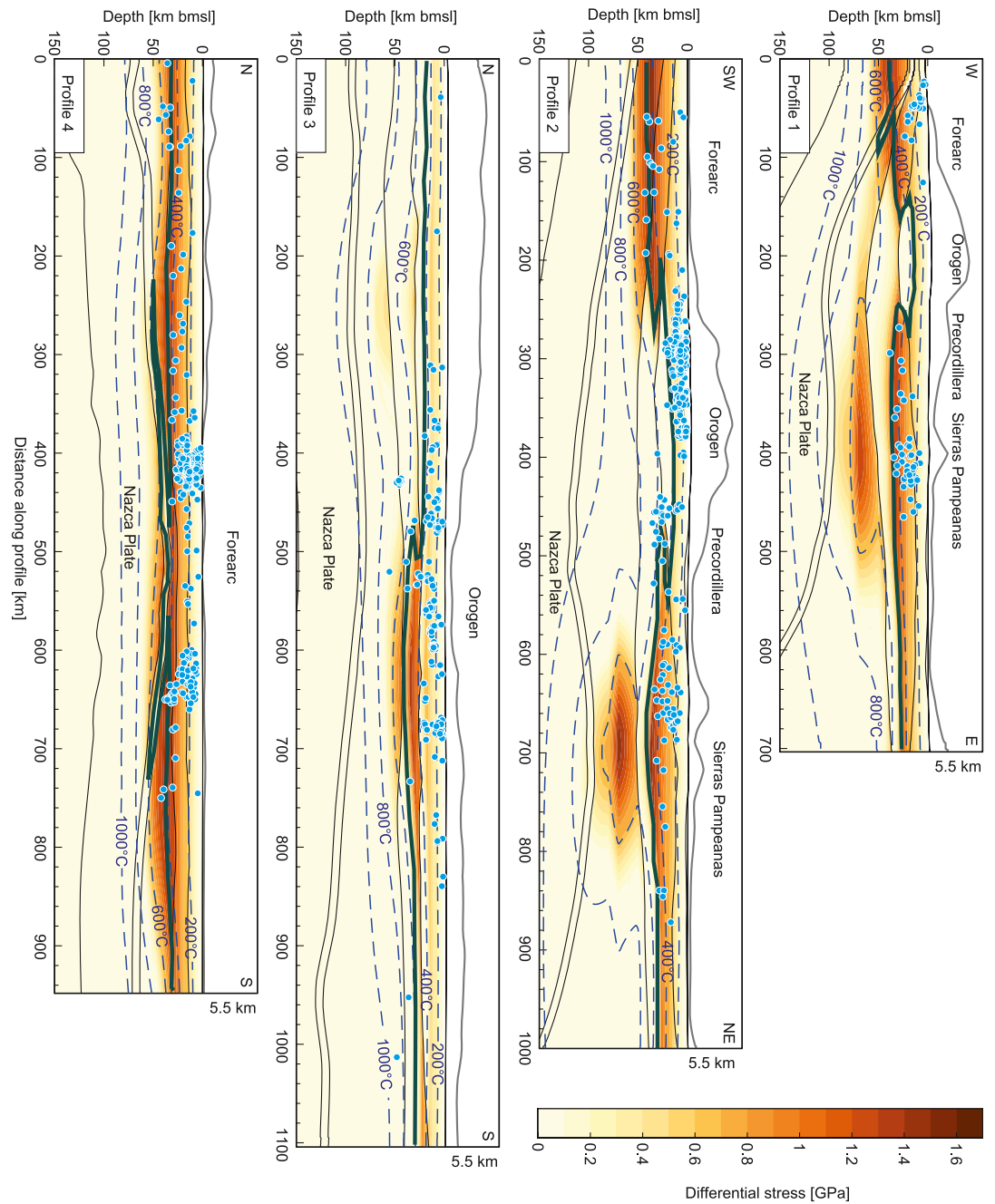
Figure 6. Differential stress computed along cross-sections 1–4 indicated in Figure 1. Light-blue dots show the location of hypocenters of seismic events within 5 km from each profile. The isotherms are marked in dashed blue lines. The brittle-ductile transition is shown in a thick green line. Black lines show the interfaces of the model layers. Topographic elevations are shown on top of each profile with a vertical exaggeration of 10:1. For abbreviations of main morphotectonic provinces see Figure 1.

20–25 km depth in the upper crust (Figure 6 and Figure S5 in Supporting Information S1, Profile 1). However, the orogen depicts a local increase in strength and effective viscosity in the mantle between 500 and 800 km along the Profile 3 (1.5 GPa, Figure 6; 24–25 log Pa s and Figure S5 in Supporting Information S1). This corresponds a minimum in the temperature distribution reached at about 34°S–36°S, as also illustrated by the deepening of the 450°C and 600°C isotherms at 33°S–35°S (Figure 2). In the foreland, the strength and effective viscosity maxima are 1.5 GPa and 24 log Pa s, respectively, located at lower crustal depths of ~35 km (Figure 6 and Figure

S5 in Supporting Information S1, Profiles 1–2). Beneath the Sierras Pampeanas, the continental mantle exhibits high strength and effective viscosity values (0.6–1.5 GPa, Figure 6; 22.5–24 log Pa s, Figure S5 in Supporting Information S1; Profiles 1–2). The highest strength values in the lower crust and continental lithospheric mantle correlate spatially with a deepening in the 600°C isotherm in the northern BAF. In the mantle, low values of mechanical strength and effective-viscosity values are attained in the orogen and the remainder of the foreland (<0.5 GPa, Figure 6; 20–22 log Pa s, Figure S5 in Supporting Information S1). The oceanic plate is characterized by a higher strength (>1 GPa) and effective viscosity (>24 log Pa s) at shallow depths (<50 km) and along the flat-slab segment beneath the Precordillera and the Sierras Pampeanas (Figure 6 and Figure S5 in Supporting Information S1, Profiles 1–2 and 4).

These modeled strength heterogeneities between the different morphotectonic provinces can be also be discussed in terms of depth variations in the BDT. In the orogen, the BDT occurs at upper crustal levels while in the foreland it deepens, reaching lower crustal depths (Figure 6, Profiles 1–3). In the forearc, on the other hand, the BDT occurs within the lithospheric mantle or within the oceanic slab (Figure 5.6). Within the slab, higher differential stresses (>1 GPa) occur above ∼50 km depth in the western model domain (Figure 5.5.6a). However, in contrast to what is observed within the continental plate, there are no significant lateral strength variations within the slab.

4. Discussion

4.1. Modeled Mechanical Strength of the Lithosphere

Our results are indicative of a heterogeneous distribution of integrated lithospheric strength of the overriding continental South American plate in the different morphotectonic provinces. Mechanically strong domains are found in the forearc, the central-western part of the orogen, and the foreland areas of the Precordillera and Sierras Pampeanas, and are neighbored by contrast with a weak orogen. The remaining foreland areas display intermediate strengths.

The comparison between the 3D configuration of the thermal field and the strength variations implies that the modeled strength distribution is mainly controlled by the lithospheric thermal field: there exists a one-to-one correspondence between strengthening and weakening of the lithosphere and cold and warm domains, respectively. Given the first-order control of the temperature on the strength distribution, the depths of the isotherms can be used as a proxy for the strength of the lithosphere. More precisely, the overall rheological behavior of the lithosphere can be described by variations in the depth of the 450°C isotherm, which coincides with the BDT in most of the study area. A deepening of the 450°C isotherm down to lower-crustal or mantle levels is associated with an overall strengthening of the lithosphere, and vice versa. We note that variations in the thermal configuration are primarily controlled by the distribution of the volumetric heat contribution of the upper radiogenic crust and, to a lesser extent, by superposed cooling limited to domains around the subducting slab (Rodriguez Piceda, Scheck Wenderoth, Bott et al., 2021). Where the upper crustal layer thins out and the slab is relatively shallow (in the flat-slab segment or in proximity to the trench), temperatures are lower and the lithosphere is thus mechanically stronger.

Other controlling factors for the lithospheric strength distribution are the background strain rate and lithology-dependent mechanical rock properties. A key assumption of our approach is to approximate ductile behavior by secondary (steady-state) creep, which shows a power-law sensitivity to imposed temperatures and strain-rates. In an attempt to test the robustness of our results to variations in these parameters, we have tested two end-member model realizations in terms of imposed strain rates (Text S7 in Supporting Information S1). The alternative values of strain rate (1e−13 s^{-1} and 1e−16 s^{-1}) were chosen according to end-member values derived from GNSS velocities (Drewes & Sánchez, 2017; Kreemer et al., 2014). Within the tested interval, variations in strain rate have little effect on the overall strength distribution: higher strain-rate values lead to a slight increase in the total strength and vice versa. As expected, the model depicting the highest strain rate of 1e−13 s^{-1} differs the most with respect to the reference model (Section 3.2). In this alternative configuration, the BDT is encountered at greater depths and the lateral contrasts in integrated lithospheric strength, although still persisting, are less sharp than in the case of the reference model. This latter observation is the result of the non-linear (power-law) functional dependence of ductile rock deformation with temperature: with increasing temperatures, the effect of varying the

imposed strain rate is larger than at lower temperature conditions. Interestingly, variations in imposed strain-rate values do not affect the spatial distribution of coupling conditions between the continental crust and the mantle.

To evaluate the effect of variations in rock properties on the resulting strength, we selected an alternative composition for the lower crust, the latter being the layer with the least observational constraints on lithological composition of all the model units (Table 1; Rodriguez Piceda, Scheck Wenderoth, Gomez Dacal et al., 2021). Gravity-constrained densities (3,100 kgm^{-3}, Rodriguez Piceda, Scheck Wenderoth, Gomez Dacal et al., 2021) and mean P-wave velocities of 6.76 km s^{-1} (Marot et al., 2014; Pesicek et al., 2012; Scarfì & Barberi, 2019) are indicative of a predominantly mafic composition of the lower crust. Accordingly, we opted for ''dry diabase'' (Afonso & Ranalli, 2004) as opposed to ''dry mafic granulite'' (Wilks & Carter, 1990, Table 1) as an alternative rheology. Although the alternative model with a dry diabase depicts higher strength values, the overall trends in the lateral distribution of integrated crustal and lithospheric strength are not affected by this choice (Text S8 in Supporting Information S1). The highest horizontal gradient again occurs at the transition between the orogen and the foreland and between the orogen and the forearc, an observation that provide confidence in the reliability of the conclusions drawn from the rheological modeling.

The trends in the modeled lateral variability of integrated lithospheric strength found in our study (Figures 5a-5b) can be qualitatively compared with previous elastic thickness estimates (Te), derived from a cross-correlation between topography and Bouguer gravity anomaly (Astort et al., 2019; Ibarra & Prezzi, 2019; Nacif et al., 2017; Sánchez et al., 2018; Tassara & Yáñez, 2003). High values of Te usually are indicative of a strong lithosphere, whereas low values of Te correspond to a weaker lithosphere (e.g., Burov, 2011; Burov & Diament, 1995; Watts & Burov, 2003). Accordingly, Te values of 40–60 km are consistent with the cold and strong areas of the forearc, the central-western part of the orogen and the northern part of the foreland. Te values of less than 30 km correspond to warmer and weaker areas of the orogen and the central-southern BAF. Likewise, north of our study area, at the latitudes of the Andean Plateau (Altiplano-Puna Plateau; 21°S–28°S), Ibarra and Prezzi (2019) and Meeβen (2019) found a similar spatial correlation between the different morphotectonic provinces and the strength distribution within the continental lithosphere. They consistently encountered a mechanically weak orogenic domain that contrasts with the mechanically strong forearc and BAF regions. We can therefore conclude that the contrasting rheological characteristics between the forearc, orogen, and BAF regions are a distinct signature of the Central Andes. The open question of whether this characteristic also applies to other non-collisional orogens could addressed in future investigations.

4.2. Implications of Modeled Plate Strength for Upper-Plate Seismicity

One main outcome of our study is the recognition of the spatial correlation between the modeled brittle domain of the continental plate and the observed depth of the seismicity, with maximum depths of hypocenters increasing where the BDT deepens (forearc and northern BAF; Figure 6). We can consider this result as robust since at depths greater than the modeled BDT, the onset of thermally activated viscous creep would lead to a more diffusive pattern of deformation, thus preventing strain localization, weakening and associated seismicity to occur (Handy & Brun, 2004). This observation in turn suggests that the depth of the BDT derived from our rheological model can be considered as a first-order approximation of the lower bound of the seismogenic zone in the study region. This conclusion is consistent with previous studies that compared computed YSEs of the continental lithosphere with depth-frequency distributions of hypocenters (Anikiev et al., 2020; Chen & Molnar, 1983; Doglioni et al., 2011; Ibarra et al., 2021; Petricca et al., 2018; Rolandone et al., 2004).

We also found a spatial correlation between the modeled integrated strength and upper-plate seismicity in terms of their distribution with respect to the boundaries between the different morphotectonic provinces. Upper-plate seismicity tends to localize along the boundaries between cold and strong domains (the forearc, the central-western part of the orogen and the northern part of the BAF), whereas the warm and weak morphotectonic provinces (most of the orogen and BAF) are generally characterized by a lack of upper-plate seismicity. However, lack of a dense seismological instrumentation in this part of the Andean orogen could also partly contribute to the low seismicity rate observed in the area. This relationship between modeled integrated strength and upper plate seismicity indicates that the mechanically stronger domains can efficiently resist internal deformation and can effectively transmit accumulated stresses to their edges, where the presence of a sharp lateral decay in lithospheric strength causes slip instability to develop, thereby possibly triggering seismic rupture. This conclusion corroborates recent

findings by Ibarra et al. (2021), who proposed that upper-plate seismicity is restricted to the areas with high horizontal gradients of integrated strength at the transition from warm and weak to cold and strong crustal domains. The presence of a causative relationship between lateral rheological heterogeneities and strain localization has also been proposed as an explanation for the establishment and preservation over (geological) time of long-term deformation patterns in the lithosphere. For example, Calignano et al. (2015) through analogue modeling, argued that strain localizes at the margins of strong lithospheric domains, whereas the mechanically strong domains themselves are only affected by minor deformation.

A factor that could contribute to the aseismic character of the northern part of the Andean orogen is the increase in the gravitational potential energy (GPE) due to high elevations and large crustal thicknesses (cf. Figures 1 and 2b). An increase in GPE would prevent any internal contractional deformation of the orogen and would favor lateral transmission of compressional stresses to adjacent areas of lower GPE (i.e., the forearc and the BAF), which, depending on their lithospheric strength, could accumulate stresses, that could subsequently be released coseismically (Mareschal & Jaupart, 2011; Stüwe, 2007). If the GPE surpasses a certain threshold, then this increase could lead to gravitational collapse of the orogen (e.g., Chen & Molnar, 1983; Molnar & Tapponnier, 1975). However, there is no evidence that this process is currently taking place in the Andean Orogen at the latitudes of the study area, based on the lack of observed extensional neotectonic structures. To test if the GPE could contribute to the scarce observed seismicity in this part of the orogen, we computed the GPE values from the load distribution of our 3D density model and compared these values with the pattern of upper-plate seismicity (Text S9 in Supporting Information S1). We found that the northern part of the orogen is indeed characterized by high GPE values (>6.36e14 Nm^{-1}) and that this domain is generally devoid of seismic activity; instead, seismicity is localized within the eastern boundary, which is characterized by a sharp decay in GPE (<6.3e14 Nm^{-1}). In other model areas (such as the BAF and forearc regions), however, there is no evident spatial correlation between GPE magnitudes and earthquake distributions: seismic events are recorded across areas with both high and low GPE values. Hence, in these areas, internal sources of stress are less suitable to explain the seismic deformation patterns than integrated strength variations.

The observed spatial correlation between upper-plate seismicity and sharp horizontal gradients in mechanical strength of the lithosphere breaks in the northern parts of the foreland. Here, seismic activity occurs in the interiors of a cold and strong lithospheric domain (Figures 5a and 5b) and where the crust and mantle are mechanically coupled (Figure 5d). We should additionally note that in this region the upper crustal strength far exceeds magnitudes considered typical for tectonic stresses (100–600 MPa; e.g., Burov, 2011; Cloetingh & Wortel, 1986; Molnar & Lyon-Caen, 1988), which apparently contradicts the observed active deformation in the area. In addition, the seismogenic depth here attains depths of 30–40 km, which is unusually large for crustal earthquakes (e.g., Maggi et al., 2000). By analyzing the moment magnitude (Mw) of the earthquakes, we note that seismicity in this domain also include upper-plate events with the highest magnitudes (Mw > 6; Text S10 in Supporting Information S1). These observations raise the question as to what underlying mechanism could promote the observed localization of deep, high-magnitude seismicity in a region that should instead resist to active deformation. It is possible that our model overestimates the integrated strength in this region. A reduction in strength could be due to higher temperatures, lower strain rate and/or weaker rheological properties. However, observed trends in the distribution of lithospheric strength are not highly sensitive to variations in these parameters (Text S7 and S8 in Supporting Information S1). With respect to the thermal field, a wide range of observations independent of our study, including seismic tomography (Marot et al., 2014; Wagner et al., 2005) and wellbore temperature and heat flow measurements (Collo et al., 2018; Hamza & Muñoz, 1996), indicate that the lithosphere in the northern foreland is significantly colder than its southern counterpart and the orogen. This also agrees with other modeling studies of the Sierras Pampeanas lithosphere (Ibarra et al., 2021; Meeβen, 2019). Furthermore, the characteristics of the recorded seismicity (deep and high-magnitude events) may be themselves indicative of the presence underneath this area of a strong lithosphere. The observed deepening of events at ∼40 km depth indicates a consequent deepening of brittle conditions, which can be related to a cold and/or has strong crust (e.g., mafic granulite) composition (Craig & Jackson, 2021; Jackson et al., 2008; Maggi et al., 2000; Pérez Luján et al., 2015). These features are consistent with modeled variations in temperatures (Rodriguez Piceda, Scheck Wenderoth, Bott et al., 2021) and thickness of the mafic lower crust modeled by Rodriguez Piceda, Scheck Wenderoth, Gomez Dacal et al. (2021) (Figures 2d and 3). Indeed, high-magnitude earthquakes as recorded in this area are compatible with a stronger lithosphere that is able to store elastic energy over longer time to be finally released
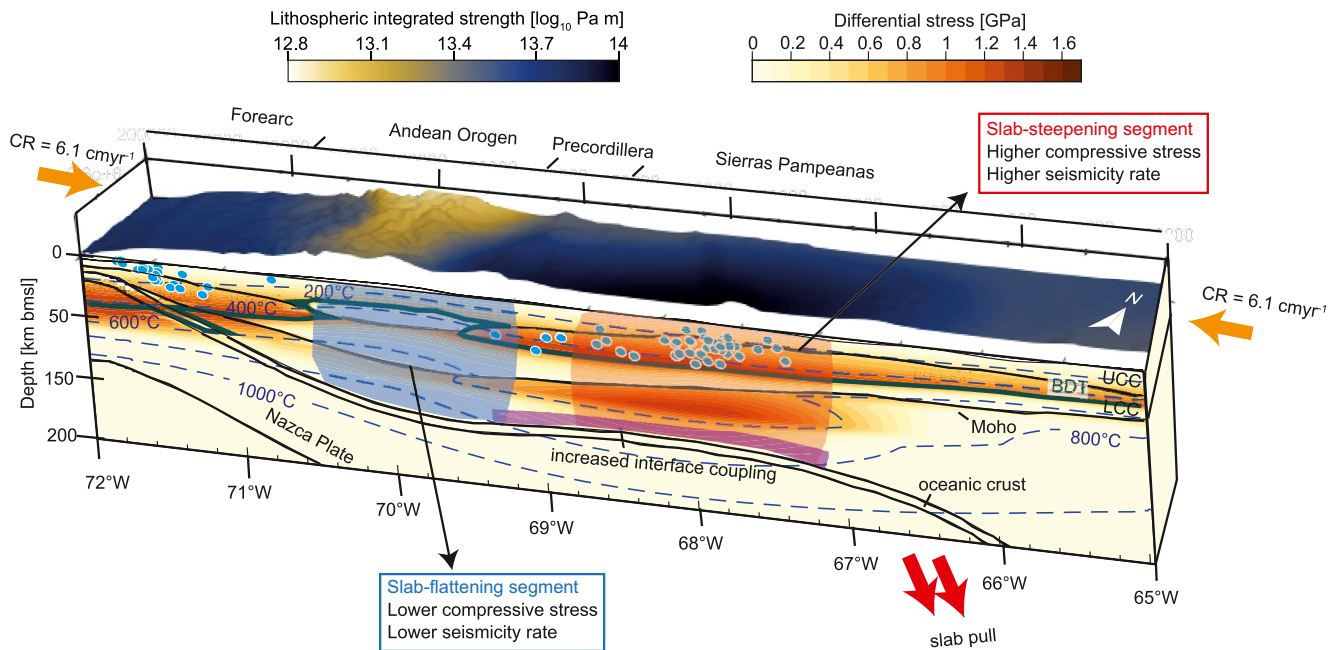
Figure 7. Schematic profile of integrated lithospheric strength and differential stress at the latitudes of the flat-slab segment (same location as profile one; cf. Figure 1) showing the proposed role of the slab-dip geometry in the localization of upper-plate seismicity (light-blue dots). Transmission of stresses occurs along the subduction interface due to increased plate coupling, but the flat slab prevents internal deformation above most of the subhorizontal segment (flattening segment; blue-shaded area), as proposed by Martinod et al. (2020). Compressional deformation occurs in the transition zone between the flat and steep sectors of the slab, promoted by increased slab pull (steepening segment; red-shaded area). The isotherms (Rodriguez Piceda, Scheck Wenderoth, Bott et al., 2021) are marked by dashed blue lines. Light-gray lines show the interfaces of the model layers (Rodriguez Piceda, Scheck Wenderoth, Gomez Dacal et al., 2021). CR = convergence rate; UCC: Upper continental crust; LCC: lower continental crust.

in high-magnitude events. From all these observations, we can therefore conclude that the presence of a strong, seismically active lithosphere in the northern foreland is a robust feature.

To explain the occurrence of seismicity in the northern foreland, one possible scenario is that seismic rupture occurs where the strong lithosphere is locally weakened due to the presence of crustal-scale discontinuities in the form of terrane sutures associated with pre-Andean collisional events, as proposed by Meeβen (2019) and Ibarra et al. (2021). According to this interpretation, we would expect to find a similar density of seismicity in regions where such heterogeneities are observed, such as in the Sierras Pampeanas (Figure 1). The observed seismicity pattern, however, there is more complex, with a higher density of seismic events encountered mainly within a sector of the Sierras Pampeanas between 31°S and 33°S and 67°W–69°W than in the remains of the morphotectonic province, which, in turn, is characterized by a more sparse seismicity (Figure 4a; e.g., Alvarado Barrientos et al., 2009; Alvarado, Pardo et al., 2009; Richardson et al., 2012).

A second possible scenario is to consider that this seismically active region can be subjected to other sources of stress as those from plate convergence, such as stresses related to a negative buoyancy of the slab where it transitions to a steep angle to the east and to the south (''slab steepening''; Figure 7). When comparing the upper-plate seismicity pattern with the geometry of the slab in the SCA, the epicentral distribution shows a triangular shape where the E–W extent of the seismically active area narrows from north to south, resembling E–W variations in the width of the flat-slab segment along the strike of the subduction zone (Figure 4). In particular, active seismic deformation away from the trench appears to cluster toward the south and east where the slab shifts from a sub-horizontal to a steep-dip configuration (''steepening segment'', below the Sierras Pampeanas and in a narrow corridor below the Cuyo basin and the central-western part of the orogen; cf. Figure 4). Similar observations were also made in previous studies (Espurt et al., 2008; Pardo et al., 2002). In contrast, only minor seismic deformation is observed in the northern orogen, that is, inside the flat-slab segment far from where it resumes its steepening (cf. Figure 4). In line with these observations, we propose that stresses related to geometrical variations across the slab surface are likely an additional controlling factor of upper-plate seismicity in the region.

The question of whether a causative relationship between stresses related to the negative buoyancy of the slab and localization of upper-plate deformation exists has been addressed by several studies in the north of the SCA, at the latitudes of the Altiplano-Puna Plateau (15°S–28°S; Gutscher, 2002, 2018; Horton, 2018; Jordan et al., 1983; Martinod et al., 2020; Ramos & Folguera, 2009). For instance, Martinod et al. (2020), by means of geodynamic modeling, systematically analyzed how the dip geometry of the slab influences the magnitude and distribution of effective stresses in the overriding plate during episodes of flat subduction. According to their model, maximum compressive stresses are shifted eastwards during flat-subduction stages because of two active mechanisms: (a) increased friction applied by the subducting oceanic plate to the continental plate, and (b) amplified negative buoyancy of the slab once the oceanic plate resumes steep subduction (Figure 7). As a result, maximum effective stresses localize above the steepening segment of the slab (i.e., in a transition zone between the flat and steep slab). This contrasts to the minor deformation in the remaining parts of the flat slab segment, where continental and oceanic plates are mechanically coupled. In the SCA, the modeled rheological characteristics and the seismicity pattern in the upper plate are consistent with the model proposed by Martinod et al. (2020), suggesting that similar mechanisms could be active also in our study region. Therefore, our investigation would favor a hypothesis where the flat slab generally preserves the lithosphere from deformation, and seismicity mainly localizes where the slab returns to a steep subduction angle, both to the west and south (Figure 7). Geodynamic modeling experiments integrating the present-day geometry, density and thermal configuration of the SCA are required to further test this hypothesis and to constrain magnitudes of dynamic stresses in the oceanic and continental plates.

A varying slab geometry could have a secondary effect in the localization of seismic upper-plate deformation. In the flat slab domain, the continental and oceanic lithosphere are cold and strong; in the transition to steep subduction, the oceanic lithosphere successively heats up and weakens, thus the integrated lithospheric strength also decreases (cf. Figure 5). Regions where such lateral contrasts in integrated lithospheric strength occur, would also be more prone to localized deformation.

5. Conclusions

In this contribution, we computed the long-term yield strength of the lithosphere and compared it with the seismicity distribution within the continental South American Plate of the SCA. We identified lateral variations in integrated strength, which correlate spatially with the main morphotectonic provinces. In this scenario the Andean orogen is mechanically weaker compared to the adjacent forearc and foreland regions. In the majority of these domains, the bulk of the lithospheric strength resides in the crust, with the exception of the forearc and the Sierras Pampeanas.

There is a spatial correlation between the strength configuration and the intraplate seismicity pattern over a large portion of the study area, with the BDT effectively bounding the depth extent of the seismogenic zone in the SCA. Deeper and high-magnitude hypocenters are found in areas characterized by a cold a mechanically strong lithosphere with a large mechanical thickness (forearc and northern BAF). Most of the intraplate seismicity localizes at the boundaries between weak and strong domains. This indicates that stresses are effectively transmitted from the mechanically strong to the weak parts of the lithosphere, where the bulk of the seismic deformation occurs. Deep intraplate seismicity of high-magnitude in the strong lithosphere of the Precordillera and the Sierras Pampeanas might be explained by the added effects of: (a) enhanced coupling between the oceanic and continental plates due to the cold and strong lithosphere above the flat slab and (b) increased negative buoyancy in the steepening segment of the slab. In addition, the characteristics of the earthquakes in this region (i.e., great depths and high Mw) are compatible with a mechanically strong crust resulting from the superposed effect of cold temperatures and large lower crustal thickness.

Data Availability Statement

References

Afonso, J. C., & Ranalli, G. (2004). Crustal and mantle strengths in continental lithosphere: Is the jelly sandwich model obsolete? *Tectonophysics*, *394*(3–4), 221–232. https://doi.org/10.1016/j.tecto.2004.08.006

Allmendinger, R. W., Ramos, V. A., Jordan, T. E., Palma, M., & Isacks, B. L. (1983). Paleogeography and Andean structural geometry, northwest Argentina. *Tectonics*, *2*(1), 1–16. https://doi.org/10.1029/TC002i001p00001

Alvarado, P., Barrientos, S., Saez, M., Astroza, M., & Beck, S. (2009). Source study and tectonic implications of the historic 1958 Las Melosas crustal earthquake, Chile, compared to earthquake damage. *Physics of the Earth and Planetary Interiors*, *175*(1), 26–36. https://doi.org/10.1016/j.pepi.2008.03.015

Alvarado, P., & Beck, S. (2006). Source characterization of the San Juan (Argentina) crustal earthquakes of 15 January 1944 (Mw 7.0) and 11 June 1952 (Mw 6.8). *Earth and Planetary Science Letters*, *243*(3), 615–631. https://doi.org/10.1016/j.epsl.2006.01.015

Alvarado, P., Beck, S., Zandt, G., Araujo, M., & Triep, E. (2005). Crustal deformation in the south-central Andes backarc terranes as viewed from regional broad-band seismic waveform modelling. *Geophysical Journal International*, *163*(2), 580–598. https://doi.org/10.1111/j.1365-246X.2005.02759.x

Alvarado, P., Pardo, M., Gilbert, H., Miranda, S., Anderson, M., Saez, M., & Beck, S. (2009). Flat-slab subduction and crustal models for the seismically active Sierras Pampeanas region of Argentina. In S. M. Kay, V. A. Ramos, & W. R. Dickinson (Eds.), *Backbone of the Americas: Shallow subduction, plateau uplift, and ridge and terrane collision*. Geological Society of America. https://doi.org/10.1130/2009.1204(12)

Alvarado, P., Sánchez, G., Saez, M., & Castro de Machuca, B. (2010). Nuevas evidencias de la actividad sísmica del terreno Cuyania en la región de subducción de placa horizontal de Argentina. *Revista Mexicana de Ciencias Geológicas*, *27*(2), 278–291.

Amante, C., & Eakins, B. (2009). *ETOPO1 1 arc-minute global relief model: Procedures, data Sources and analysis (NOAA technical memorandum NESDIS NGDC-24)*. National Geophysical Data Center, NOAA. https://doi.org/10.7289/V5C8276M

Ammirati, J., Vargas, G., Rebolledo, S., Abrahami, R., Potin, B., Leyton, F., & Ruiz, S. (2019). The crustal seismicity of the Western andean thrust (Central Chile, 33°–34° S): Implications for regional tectonics and seismic hazard in the santiago area. *Bulletin of the Seismological Society of America*, *109*(5), 1985–1999. https://doi.org/10.1785/0120190082

Ammirati, J.-B., Alvarado, P., Perarnau, M., Saez, M., & Monsalvo, G. (2013). Crustal structure of the Central Precordillera of San Juan, Argentina (31°S) using teleseismic receiver functions. *Journal of South American Earth Sciences*, *46*, 100–109. https://doi.org/10.1016/j.jsames.2013.05.007

Ammirati, J.-B., Pérez Luján, S., Alvarado, P., Beck, S., Rocher, S., & Zandt, G. (2016). High-resolution images above the Pampean flat slab of Argentina (31–32°S) from local receiver functions: Implications on regional tectonics. *Earth and Planetary Science Letters*, *450*, 29–39. https://doi.org/10.1016/j.epsl.2016.06.018

Anderson, M., Alvarado, P., Zandt, G., & Beck, S. (2007). Geometry and brittle deformation of the subducting Nazca Plate, Central Chile and Argentina. *Geophysical Journal International*, *171*(1), 419–434. https://doi.org/10.1111/j.1365-246X.2007.03483.x

Anikiev, D., Cacace, M., Bott, J., Gomez Dacal, M. L., & Scheck-Wenderoth, M. (2020). Influence of lithosphere rheology on seismicity in an intracontinental rift: The case of the rhine graben. *Frontiers of Earth Science*, *8*. https://doi.org/10.3389/feart.2020.592561

Araneda, M., Asch, G., Bataille, K., Bohm, M., Bruhn, C., Giese, P., et al. (2003). A crustal model along 39°S from a seismic refraction profile-ISSA 2000. *Revista Geologica de Chile*, *30*(1), 83–101. https://doi.org/10.4067/S0716-02082003000100006

Assumpção, M., Feng, M., Tassara, A., & Julià, J. (2013). Models of crustal thickness for South America from seismic refraction, receiver functions and surface wave tomography. *Tectonophysics*, *609*, 82–96. https://doi.org/10.1016/j.tecto.2012.11.014

Astini, R., Benedetto, J., & Vaccari, N. (1995). The early paleozoic evolution of the Argentine precordillera as a laurentian rifted, drifted, and collided terrane: A geodynamic model. *The Geological Society of America Bulletin*, *107*, 253–273. https://doi.org/10.1130/0016-7606(1995)107<0253:TEPEOT>2.3.CO;2

Astort, A., Colavitto, B., Sagripanti, L., García, H., Echaurren, A., Soler, S., et al. (2019). Crustal and mantle structure beneath the southern Payenia volcanic province using gravity and magnetic data. *Tectonics*, *38*(1), 144–158. https://doi.org/10.1029/2017TC004806

Azcuy, C., & Caminos, R. (1987). El Sistema Carbonifero en la Republica Argentina. Diastrofismo. In *El sistema carbonífero en la República Argentina* (pp. 239–251). Academia Nacional de Ciencias.

Boyce, D., Charrier, R., & Farías, M. (2020). The first andean compressive tectonic phase: Sedimentologic and structural analysis of mid-cretaceous deposits in the coastal cordillera, Central Chile (32°50′S). *Tectonics*, *39*(2). https://doi.org/10.1029/2019TC005825

Burov, E., & Diament, M. (1995). The effective elastic thickness (Te) of continental lithosphere: What does it really mean? *Journal of Geophysical Research*, *100*(B3), 3905–3927. https://doi.org/10.1029/94JB02770

Burov, E. B. (2011). Rheology and strength of the lithosphere. *Marine and Petroleum Geology*, *28*(8), 1402–1443. https://doi.org/10.1016/j.marpetgeo.2011.05.008

Byerlee, J. D. (1968). Brittle-ductile transition in rocks. *Journal of Geophysical Research*, *73*(14), 4741–4750. https://doi.org/10.1029/JB073i014p04741

Cacace, M., & Scheck-Wenderoth, M. (2016). Why intracontinental basins subside longer: 3-D feedback effects of lithospheric cooling and sedimentation on the flexural strength of the lithosphere: Subsidence at intracontinental basins. *Journal of Geophysical Research: Solid Earth*, *121*(5), 3742–3761. https://doi.org/10.1002/2015JB012682

Calignano, E., Sokoutis, D., Willingshofer, E., Gueydan, F., & Cloetingh, S. (2015). Strain localization at the margins of strong lithospheric domains: Insights from analog models. *Tectonics*, *34*(3), 396–412. https://doi.org/10.1002/2014TC003756

Chen, K., Liu, Z., & Song, Y. T. (2020). Automated GNSS and teleseismic earthquake inversion (AutoQuake inversion) for tsunami early warning: Retrospective and real-time results. *Pure and Applied Geophysics*, *177*(3), 1403–1423. https://doi.org/10.1007/s00024-019-02252-x

Chen, W.-P., Hung, S.-H., Tseng, T.-L., Brudzinski, M., Yang, Z., & Nowack, R. L. (2012). Rheology of the continental lithosphere: Progress and new perspectives. *Tectonic Evolution of Tibet and Surrounding Regions*, *21*(1), 4–18. https://doi.org/10.1016/j.jgr.2011.07.013

Chen, W.-P., & Molnar, P. (1983). Focal depths of intracontinental and intraplate earthquakes and their implications for the thermal and mechanical properties of the lithosphere. *Journal of Geophysical Research: Solid Earth*, *88*, 4183–4214. https://doi.org/10.1029/JB088iB05p04183

Cloetingh, S., & Wortel, R. (1986). Stress in the Indo-Australian plate. *Tectonophysics*, *132*(1), 49–67. https://doi.org/10.1016/0040-1951(86)90024-7

Cloos, M., & Shreve, R. L. (1996). Shear-zone thickness and the seismicity of Chilean- and Marianas-type subduction zones. *Geology*, *24*(2), 107–110. https://doi.org/10.1130/0091-7613(1996)024<0107:SZTATS>2.3.CO;2

Collo, G., Ezpeleta, M., Dávila, F. M., Giménez, M., Soler, S., Martina, F., et al. (2018). Basin thermal structure in the Chilean-pampean flat subduction zone. In *The evolution of the Chilean-argentinean Andes* (pp. 537–564). Springer.

Contreras-Reyes, E., Grevemeyer, I., Flueh, E. R., & Reichert, C. (2008). Upper lithospheric structure of the subduction zone offshore of southern Arauco peninsula, Chile, at ~38°S. *Journal of Geophysical Research*, *113*, B07303. https://doi.org/10.1029/2007JB005569

Copernicus Climate Change Service (C3S). (2019). *ERA5-Land monthly averaged data from 1981 to present*. https://doi.org/10.24381/cds68d2bb3

Costa, C., Alvarado, A., Audemard, F., Audin, L., Benavente, C., Bezerra, F. H., et al. (2020). Hazardous faults of South America; compilation and overview. *Journal of South American Earth Sciences*, *104*, 102837. https://doi.org/10.1016/j.jsames.2020.102837

Costa, C., Machette, M., Dart, R., Bastia, H., Paredes, J., Perucca, L., et al. (2000). *Map and database of Quaternary faults and folds in Argentina (Open-File Report No. 00–0108)* (p. 76). U.S. Geological Survey.

Craig, T. J., & Jackson, J. A. (2021). Variations in the seismogenic thickness of east Africa. *Journal of Geophysical Research: Solid Earth*, *126*(3), e2020JB020754. https://doi.org/10.1029/2020JB020754

Crameri, F. (2021). Scientific colour maps. Version 7.0.0. *Zenodo*. https://doi.org/10.5281/zenodo.4491293

del Papa, C., Hongn, F., Powell, J., Payrola, P., Do Campo, M., Strecker, M. R., et al. (2013). Middle eocene-oligocene broken-foreland evolution in the andean calchaqui valley, NW Argentina: Insights from stratigraphic, structural and provenance studies. *Basin Research*, *25*(5), 574–593. https://doi.org/10.1111/bre.12018

Doglioni, C., Barba, S., Carminati, E., & Riguzzi, F. (2011). Role of the brittle–ductile transition on fault activation. *Physics of the Earth and Planetary Interiors*, *184*(3–4), 160–171. https://doi.org/10.1016/j.pepi.2010.11.005

Drewes, H., & Sánchez, L. (2017). *The varying surface kinematics in Latin America: VEMOS 2009, 2015, and 2017*. Presented at the Symposium SIRGAS2017.

Dziewonski, A. M., Chou, T.-A., & Woodhouse, J. H. (1981). Determination of earthquake source parameters from waveform data for studies of global and regional seismicity. *Journal of Geophysical Research: Solid Earth*, *86*, 2825–2852. https://doi.org/10.1029/JB086iB04p02825

Ekström, G., Nettles, M., & Dziewoński, A. M. (2012). The global CMT project 2004–2010: Centroid-moment tensors for 13,017 earthquakes. *Physics of the Earth and Planetary Interiors*, *200–201*, 1–9. https://doi.org/10.1016/j.pepi.2012.04.002

Espurt, N., Funiciello, F., Martinod, J., Guillaume, B., Regard, V., Faccenna, C., & Brusset, S. (2008). Flat subduction dynamics and deformation of the South American plate: Insights from analog modeling. *Tectonics*, *27*(3). https://doi.org/10.1029/2007TC002175

Farías, M., Charrier, R., Carretier, S., Martinod, J., Fock, A., Campbell, D., et al. (2008). Late Miocene high and rapid surface uplift and its erosional response in the Andes of central Chile (33°–35°S). *Tectonics*, *27*(1). https://doi.org/10.1029/2006TC002046

Fennell, L. M., Folguera, A., Naipauer, M., Gianni, G., Rojas Vera, E. A., Bottesi, G., & Ramos, V. A. (2015). Cretaceous deformation of the southern central Andes: Synorogenic growth strata in the Neuquén group (35° 30′–37° S). *Basin Research*, *29*, 51–72. https://doi.org/10.1111/bre.12135

Giambiagi, L., Mescua, J., Bechis, F., Tassara, A., & Hoke, G. (2012). Thrust belts of the southern Central Andes: Along-strike variations in shortening, topography, crustal geometry, and denudation. *The Geological Society of America Bulletin*, *124*(7–8), 1339–1351. https://doi.org/10.1130/B30609.1

Giambiagi, L. B., Ramos, V. A., Godoy, E., Alvarez, P. P., & Orts, S. (2003). Cenozoic deformation and tectonic style of the Andes, between 33° and 34° south latitude. *Tectonics*, *22*(4). https://doi.org/10.1029/2001TC001354

Gleason, G. C., & Tullis, J. (1995). A flow law for dislocation creep of quartz aggregates determined with the molten salt cell. *30 Years of Tectonophysics a Special Volume in Honour of Gerhard Oertel*, *247*(1), 1–23. https://doi.org/10.1016/0040-1951(95)00011-B

Goes, S., Govers, R., Vacher, P. (2000). Shallow mantle temperatures under Europe from P and S wave tomography. *Journal of Geophysical Research: Solid Earth*, *105*, 11153–11169. https://doi.org/10.1029/1999JB900300

Goetze, C., & Evans, B. (1979). Stress and temperature in the bending lithosphere as constrained by experimental rock mechanics. *Geophysical Journal International*, *59*(3), 463–478. https://doi.org/10.1111/j.1365-246X.1979.tb02567.x

Goetze, C., Poirier, J. P., Kelly, A., Cook, A. H., & Greenwood, G. W. (1978). The mechanisms of creep in olivine. *Philosophical Transactions of the Royal Society of London - Series A: Mathematical and Physical Sciences*, *288*(1350), 99–119. https://doi.org/10.1098/rsta.1978.0008

Gregori, S. D., & Christiansen, R. (2018). Seismic hazard analysis for central-Western Argentina. *Seismological Advances in Latin America*, *9*(1), 25–33. https://doi.org/10.1016/j.geog.2017.07.006

Grimaldi, G. O., & Dorobek, S. L. (2011). Fault framework and kinematic evolution of inversion structures: Natural examples from the Neuquén Basin, Argentina. *AAPG Bulletin*, *95*(1), 27–60. https://doi.org/10.1306/06301009165

Gutscher, M.-A. (2002). Andean subduction styles and their effect on thermal structure and interplate coupling. *Journal of South American Earth Sciences*, *15*(1), 3–10. https://doi.org/10.1016/S0895-9811(02)00002-0

Gutscher, M.-A. (2018). Scraped by flat-slab subduction. *Nature Geoscience*, *11*(12), 889–890. https://doi.org/10.1038/s41561-018-0270-x

Hackney, R. I., Echtler, H. P., Franz, G., Götze, H.-J., Lucassen, F., Marchenko, D., et al. (2006). The segmented overriding plate and coupling at the south-central Chilean margin (36–42°S). In O. Oncken, G. Chong, G. Franz, P. Giese, H.-J. Götze, V. A. Ramos, et al. (Eds.), *The Andes* (pp. 355–374). Springer Berlin Heidelberg. https://doi.org/10.1007/978-3-540-48684-8_17

Hamza, V. M., & Muñoz, M. (1996). Heat flow map of South America. *Geothermics*, *25*(6), 599–646. https://doi.org/10.1016/S0375-6505(96)00025-9

Handy, M. R., & Brun, J.-P. (2004). Seismicity, structure and strength of the continental lithosphere. *Earth and Planetary Science Letters*, *223*(3–4), 427–441. https://doi.org/10.1016/j.epsl.2004.04.021

Hayes, G. P., Moore, G. L., Portner, D. E., Hearne, M., Flamme, H., Furtney, M., & Smoczyk, G. M. (2018). Slab2, a comprehensive subduction zone geometry model. *Science*, *362*(6410), 58–61. https://doi.org/10.1126/science.aat4723

Hirth, G., & Kohlstedt, D. L. (1996). Water in the oceanic upper mantle: Implications for rheology, melt extraction and the evolution of the lithosphere. *Earth and Planetary Science Letters*, *144*(1), 93–108. https://doi.org/10.1016/0012-821X(96)00154-9

Hongn, F., Mon, R., Petrinovic, I., del Papa, C., & Powell, J. (2010). Inversión y reactivación tectónicas cretácico-cenozoicas en el noroeste argentino: Influencia de las heterogeneidades del basamento neoproterozoico-paleozoico inferior. *Revista de la Asociación Geológica Argentina*, *66*(1–2), 38–53.

Hongn, F., del Papa, C., Powell, J., Petrinovic, I., Mon, R., & Deraco, V. (2007). Middle Eocene deformation and sedimentation in the Puna-Eastern Cordillera transition (23°-26°S): Control by preexisting heterogeneities on the pattern of initial Andean shortening. *Geology*, *35*(3), 271–274. https://doi.org/10.1130/G23189A.1

Horton, B. K. (2018). Sedimentary record of Andean mountain building. *Earth-Science Reviews*, *178*, 279–309. https://doi.org/10.1016/j.earscirev.2017.11.025

Ibarra, F., & Prezzi, C. B. (2019). The thermo-mechanical state of the Andes in the altiplano-puna region: Insights from curie isotherm and effective elastic thickness determination. *Revista de la Asociación Geológica Argentina*, *76*(4), 352–362.

Ibarra, F., Prezzi, C. B., Bott, J., Scheck-Wenderoth, M., & Strecker, M. R. (2021). Distribution of temperature and strength in the central andean lithosphere and its relationship to seismicity and active deformation. *Journal of Geophysical Research: Solid Earth*, *126*(5). https://doi.org/10.1029/2020JB021231

International Seismological Centre. (2021). *On-line bulletin*. https://doi.org/10.31905/D808B830

Jackson, J., McKenzie, D., Priestley, K., & Emmerson, B. (2008). New views on the structure and rheology of the lithosphere. *Journal of the Geological Society*, *165*(2), 453–465. https://doi.org/10.1144/0016-76492007-109

Jones, R. E., De Hoog, J. C., Kirstein, L. A., Kasemann, S. A., Hinton, R., Elliott, T., & Litvak, V. D. (2014). Temporal variations in the influence of the subducting slab on Central Andean arc magmas: Evidence from boron isotope systematics. *Earth and Planetary Science Letters*, *408*, 390–401. https://doi.org/10.1016/j.epsl.2014.10.004

Jones, R. E., Kirstein, L. A., Kasemann, S. A., Dhuime, B., Elliott, T., Litvak, V. D., et al. (2015). Geodynamic controls on the contamination of Cenozoic arc magmas in the southern Central Andes: Insights from the O and Hf isotopic composition of zircon. *Geochimica et Cosmochimica Acta*, *164*, 386–402. https://doi.org/10.1016/j.gca.2015.05.007

Jones, R. E., Kirstein, L. A., Kasemann, S. A., Litvak, V. D., Poma, S., Alonso, R. N., & Hinton, R. (2016). The role of changing geodynamics in the progressive contamination of Late Cretaceous to Late Miocene arc magmas in the southern Central Andes. *Lithos*, *262*, 169–191. https://doi.org/10.1016/j.lithos.2016.07.002

Jordan, T. E., Isacks, B. L., Allmendinger, R. W., Brewer, J. A., Ramos, V. A., & Ando, C. J. (1983). Andean tectonics related to geometry of subducted Nazca plate. *The Geological Society of America Bulletin*, *94*(3), 341–361. https://doi.org/10.1130/0016-7606(1983)94<341:atrtgo>2.0.co;2

Katayama, I., & Karato, S. (2008). Low-temperature, high-stress deformation of olivine under water-saturated conditions. *Physics of the Earth and Planetary Interiors*, *168*(3), 125–133. https://doi.org/10.1016/j.pepi.2008.05.019

Kay, S. M., Burns, W. M., Copeland, P., & Mancilla, O. (2006). Upper Cretaceous to Holocene magmatism and evidence for transient Miocene shallowing of the Andean subduction zone under the northern Neuquén Basin. In S. M. Kay, & V. A. Ramos (Eds.), (Vol. 407). Geological Society of America. *Evolution of an Andean Margin: A Tectonic and Magmatic View from the Andes to the Neuqueń Basin (35°-39°S lat)*. https://doi.org/10.1130/2006.2407(02)

Kay, S. M., & Mpodozis, C. (2002). Magmatism as a probe to the Neogene shallowing of the Nazca plate beneath the modern Chilean ̄at-slab. *Journal of South American Earth Sciences*, *19*.

Kley, J., & Monaldi, C. R. (2002). Tectonic inversion in the Santa Barbara System of the central Andean foreland thrust belt, northwestern Argentina. *Tectonics*, *21*(6). https://doi.org/10.1029/2002TC902003

Kley, J., Monaldi, C. R., & Salfity, J. A. (1999). Along-strike segmentation of the Andean foreland: Causes and consequences. *Tectonophysics*, *301*(1–2), 75–94. https://doi.org/10.1016/S0040-1951(98)90223-2

Kreemer, C., Blewitt, G., & Klein, E. C. (2014). A geodetic plate motion and global strain rate model. *Geochemistry, Geophysics, Geosystems*, *15*(10), 3849–3889. https://doi.org/10.1002/2014GC005407

Linkimer, L., Beck, S., Zandt, G., Alvarado, P., Anderson, M., Gilbert, H., & Zhang, H. (2020). Lithospheric structure of the Pampean flat slab region from double-difference tomography. *Journal of South American Earth Sciences*, *97*, 102417. https://doi.org/10.1016/j.jsames.2019.102417

Liu, L., & Zoback, M. D. (1997). Lithospheric strength and intraplate seismicity in the New Madrid seismic zone. *Tectonics*, *16*(4), 585–595. https://doi.org/10.1029/97TC01467

Llambias, E. J., Kleiman, L. E., & Salvarredi, J. A. (1993). El magmatismo gondwánico. In V. Ramos(Ed.), *Presented at the geología y recursos naturales de Mendoza* (pp. 53–64). Congreso Geológico Argentino.

Llambias, E. J., & Sato, A. M. (1990). El batolito de Colangüil (29-31°S) cordillera frontal de Argentina: Estructura y marco tectonico. *Andean Geology*, *17*(1), 89–108. https://doi.org/10.5027/andgeoV17n1-a04

Maggi, A., Jackson, J. A., McKenzie, D., & Priestley, K. (2000). Earthquake focal depths, effective elastic thickness, and the strength of the continental lithosphere. *Geology*, *28*(6), 495–498. https://doi.org/10.1130/0091-7613(2000)028<0495:efdeet>2.3.co;2

Maloney, K. T., Clarke, G. L., Klepeis, K. A., & Quevedo, L. (2013). The late Jurassic to present evolution of the Andean margin: Drivers and the geological record: Evolution of the andean margin. *Tectonics*, *32*(5), 1049–1065. https://doi.org/10.1002/tect.20067

Mareschal, J.-C., & Jaupart, C. (2011). Energy budget of the Earth. In H. K. Gupta (Ed.), *Encyclopedia of Solid Earth Geophysics* (pp. 285–291). Springer Netherlands. https://doi.org/10.1007/978-90-481-8702-7_64

Marot, M., Monfret, T., Gerbault, M., Nolet, G., Ranalli, G., & Pardo, M. (2014). Flat versus normal subduction zones: A comparison based on 3-D regional traveltime tomography and petrological modelling of central Chile and Western Argentina (29°–35°S). *Geophysical Journal International*, *199*(3), 1633–1654. https://doi.org/10.1093/gji/ggu355

Martino, R. D. (2003). Las fajas de deformación dúctil de las Sierras Pampeanas de Córdoba: Una reseña general. *Revista de la Asociación Geológica Argentina*, *58*(4), 549–571.

Martinod, J., Gérault, M., Husson, L., & Regard, V. (2020). Widening of the Andes: An interplay between subduction dynamics and crustal wedge tectonics. *Earth-Science Reviews*, *204*, 103170. https://doi.org/10.1016/j.earscirev.2020.103170

Meeßen, C. (2017). *VelocityConversion. V. v1.0.1. GFZ data Services*. https://doi.org/10.5880/GFZ.6.1.2017.001

Meeßen, C. (2019). *The thermal and rheological state of the Northern Argentinian foreland basins (doctoralthesis)*. Universität Potsdam. https://doi.org/10.25932/publishup-43994

Molnar, P., & Lyon-Caen, H. (1988). Some simple physical aspects of the support, structure, and evolution of mountain belts. *Geological Society of America Special Paper*, 179–208. https://doi.org/10.1130/SPE218-p179

Molnar, P., & Tapponnier, P. (1975). Cenozoic tectonics of Asia: Effects of a continental collision. *Science*, *189*(4201), 419–426. https://doi.org/10.1126/science.189.4201.419

Mon, R., & Salfity, J. (1995). *Petroleum Basins of South America* (Vol. 62). AAPG Special Volumes. Tectonic evolution of the Andes of northern Argentina

Moreno, M., Haberland, C., Oncken, O., Rietbrock, A., Angiboust, S., & Heidbach, O. (2014). Locking of the Chile subduction zone controlled by fluid pressure before the 2010 earthquake. *Nature Geoscience*, *7*(4), 292–296. https://doi.org/10.1038/ngeo2102

Moreno, M., Rosenau, M., & Oncken, O. (2010). 2010 Maule earthquake slip correlates with pre-seismic locking of Andean subduction zone. *Nature*, *467*(7312), 198–202. https://doi.org/10.1038/nature09349

Mpodozis, C., & Kay, S. M. (1990). Provincias magmáticas ácidas y evolución tectónica de Gondwana: Andes chilenos (28-31°S). *Andean Geology*, *17*(2), 153–180. https://doi.org/10.5027/andgeoV17n2-a03

Muldashev, I. (2017). *Modeling of the great earthquake seismic cycles*. Retrieved from https://publishup.uni-potsdam.de/opus4-ubp/frontdoor/index/index/docId/39892

Nacif, S., Lupari, M., Triep, E. G., Nacif, A., Álvarez, O., Folguera, A., & Gímenez, M. (2017). Change in the pattern of crustal seismicity at the Southern Central Andes from a local seismic network. *Tectonophysics*, *708*, 56–69. https://doi.org/10.1016/j.tecto.2017.04.012

Nacif, S., Triep, E., Furlani, R., & Spagnotto, S. (2013). Stripe of normal mechanisms for crustal earthquakes with M ≤ 3.5 flanking the Western side of the thrust front zone in the Andes backarc. *Natural Science*, *05*(08), 18–26. https://doi.org/10.4236/ns.2013.58A1003

Norabuena, E. O., Dixon, T. H., Stein, S., & Harrison, C. G. A. (1999). Decelerating nazca-south America and nazca-pacific plate motions. *Geophysical Research Letters*, *26*(22), 3405–3408. https://doi.org/10.1029/1999GL005394

Olivar, J., Nacif, S., Fennell, L., & Folguera, A. (2018). Within plate seismicity analysis in the segment between the high Cordillera and the Precordillera of northern Mendoza (Southern Central Andes). *Geodesy and Geodynamics*, *9*(1), 13–24. https://doi.org/10.1016/j.geog.2017.09.004

Oncken, O., Chong, G., Gerhard, F., Giese, P., Götze, H.-J., Ramos, V. A., et al. (2006). *The Andes: Active subduction orogeny*. (1st ed.). Springer-Verlag Berlin Heidelberg. Retrieved from https://www.springer.com/gp/book/9783540243298

Pardo, M., Comte, D., & Monfret, T. (2002). Seismotectonic and stress distribution in the central Chile subduction zone. *Journal of South American Earth Sciences*, *15*(1), 11–22. https://doi.org/10.1016/s0895-9811(02)00003-2

Pérez Luján, S. B., Ammirati, J.-B., Alvarado, P., & Vujovich, G. I. (2015). Constraining a mafic thick crust model in the Andean Precordillera of the Pampean flat slab subduction region. *Journal of South American Earth Sciences*, *64*, 325–338. https://doi.org/10.1016/j.jsames.2015.09.005

Pesicek, J. D., Engdahl, E. R., Thurber, C. H., DeShon, H. R., & Lange, D. (2012). Mantle subducting slab structure in the region of the 2010 M8.8 Maule earthquake (30–40°S), Chile: Mantle subducting slab structure in Chile. *Geophysical Journal International*, *191*(1), 317–324. https://doi.org/10.1111/j.1365-246X.2012.05624.x

Petricca, P., Carminati, E., Doglioni, C., & Riguzzi, F. (2018). Brittle-ductile transition depth versus convergence rate in shallow crustal thrust faults: Considerations on seismogenic volume and impact on seismicity. *Physics of the Earth and Planetary Interiors*, *284*, 72–81. https://doi.org/10.1016/j.pepi.2018.09.002

Platt, J. P., Xia, H., & Schmidt, W. L. (2018). Rheology and stress in subduction zones around the aseismic/seismic transition. *Progress in Earth and Planetary Science*, *5*(1), 24. https://doi.org/10.1186/s40645-018-0183-8

Ramos, V. A. (1988). The tectonics of the Central Andes; 30° to 33° S latitude. In S. P. Clark, Jr, B. C. Burchfiel, & J. Suppe (Eds.), (Vol. 218). Geological Society of America. https://doi.org/10.1130/SPE218-p31. Processes in Continental Lithospheric Deformation

Ramos, V. A., Cristallini, E. O., & Pérez, D. J. (2002). The pampean flat-slab of the central Andes. *Flat-Slab Subduction in the Andes*, *15*(1), 59–78. https://doi.org/10.1016/S0895-9811(02)00006-8

Ramos, V. A., & Folguera, A. (2009). Andean flat-slab subduction through time. *Geological Society, London, Special Publications*, *327*(1), 31–54. https://doi.org/10.1144/SP327.3

Ranalli, G. (1994). Nonlinear flexure and equivalent mechanical thickness of the lithosphere. *Tectonophysics*, *240*(1–4), 107–114. https://doi.org/10.1016/0040-1951(94)90266-6

Ranalli, G., & Murphy, D. C. (1987). Rheological stratification of the lithosphere. *Tectonophysics*, *132*(4), 281–295. https://doi.org/10.1016/0040-1951(87)90348-9

Richardson, T., Gilbert, H., Anderson, M., & Ridgway, K. D. (2012). Seismicity within the actively deforming eastern Sierras Pampeanas, Argentina: Seismicity in the actively deforming ESP. *Geophysical Journal International*, *188*(2), 408–420. https://doi.org/10.1111/j.1365-246X.2011.05283.x

Rivas, C., Ortiz, G., Alvarado, P., Podesta, M., & Martin, A. (2019). Modern crustal seismicity in the northern Andean Precordillera, Argentina. *Tectonophysics*, *762*, 144–158. https://doi.org/10.1016/j.tecto.2019.04.019

Rodriguez Piceda, C., Scheck Wenderoth, M., Gomez Dacal, M. L., Bott, J., Prezzi, C. B., & Strecker, M. R. (2021). Lithospheric density structure of the southern Central Andes constrained by 3D data-integrative gravity modelling. *International Journal of Earth Sciences*, *110*(7), 2333–2359. https://doi.org/10.1007/s00531-020-01962-1

Rodriguez Piceda, C., Scheck Wenderoth, M., Bott, J., Gomez Dacal, M. L., Cacace, M., Pons, M., et al. (2021). Controls of the lithospheric thermal field of an ocean-continent subduction zone: The southern central Andes. *EarthArXiv*. https://doi.org/10.31223/X5B05D

Rolandone, F., Bürgmann, R., & Nadeau, R. M. (2004). The evolution of the seismic-aseismic transition during the earthquake cycle: Constraints from the time-dependent depth distribution of aftershocks: AN evolving seismic-aseismic transition. *Geophysical Research Letters*, *31*(23). https://doi.org/10.1029/2004GL021379

Ruiz, S., & Madariaga, R. (2018). Historical and recent large megathrust earthquakes in Chile. *Tectonophysics*, *733*, 37–56. https://doi.org/10.1016/j.tecto.2018.01.015

Sagripanti, L., Colavitto, B., Jagoe, L., Andrés, F., & Costa, C. (2017). A review about the quaternary Upper-plate deformation in the southern central Andes (36–38°S): A plausible interaction between mantle dynamics and tectonics. *Journal of South American Earth Sciences*, *87*, 221–231. https://doi.org/10.1016/j.jsames.2017.11.008

Sánchez, M. A., Ariza, J. P., García, H. P., Gianni, G. M., Weidmann, M. C., Folguera, A., et al. (2018). Thermo-mechanical analysis of the Andean lithosphere over the Chilean-Pampean flat-slab region. *Journal of South American Earth Sciences*, *87*, 247–257. https://doi.org/10.1016/j.jsames.2017.09.036

Scarfì, L., & Barberi, G. (2019). New insights on the tectonic structure of the Southern Central Andes–Western Argentina–from seismic tomography. *Geology, Earth and Marine Sciences*.

Scholz, C. H. (1988). The brittle-plastic transition and the depth of seismic faulting. *Geologische Rundschau*, *77*(1), 319–328. https://doi.org/10.1007/BF01848693

Sibson, R. H. (1982). Fault zone models, heat flow, and the depth distribution of earthquakes in the continental crust of the United States. *Bulletin of the Seismological Society of America*, *72*(1), 151–163. https://doi.org/10.1785/BSSA0720010151

Smalley, R., & Isacks, B. L. (1990). Seismotectonics of thin- and thick-skinned deformation in the Andean Foreland from local network data: Evidence for a seismogenic lower crust. *Journal of Geophysical Research*, *95*, 12487. https://doi.org/10.1029/JB095iB08p12487

Smalley, R., Pujol, J., Regnier, M., Chiu, J.-M., Chatelain, J.-L., Isacks, B. L., et al. (1993). Basement seismicity beneath the Andean precordillera thin-skinned thrust belt and implications for crustal and lithospheric behavior. *Tectonics*, *12*(1), 63–76. https://doi.org/10.1029/92TC01108

Sobolev, S. V., & Babeyko, A. Y. (2005). What drives orogeny in the Andes? *Geology*, *33*(8), 617–620. https://doi.org/10.1130/G21557AR.1

Sobolev, S. V., Babeyko, A. Y., Koulakov, I., & Oncken, O. (2006). Mechanism of the andean orogeny: Insight from numerical modeling. In O. Oncken, G. Chong, G. Franz, P. Giese, H.-J. Götze, V. A. Ramos, et al. (Eds.), *The Andes: Active subduction orogeny* (pp. 513–535). Springer Berlin Heidelberg. https://doi.org/10.1007/978-3-540-48684-8_25

Stüwe, K. (2007). *Geodynamics of the lithosphere*. Springer-Verlag Berlin Heidelberg.

Tapia, F., Farías, M., Naipauer, M., & Puratich, J. (2015). Late Cenozoic contractional evolution of the current arc-volcanic region along the southern Central Andes (35°20′S). *Journal of Geodynamics*, *88*, 36–51. https://doi.org/10.1016/j.jog.2015.01.001

Tassara, A., & Yáñez, G. (2003). Relación entre el espesor elástico de la litosfera y la segmentación tectónica del margen andino (15–47°S). *Andean Geology*, *30*(2), 159–186. https://doi.org/10.4067/s0716-02082003000200002

Tesauro, M., Audet, P., Kaban, M. K., Bürgmann, R., & Cloetingh, S. (2012). The effective elastic thickness of the continental lithosphere: Comparison between rheological and inverse approaches: Te OF the continental lithosphere. *Geochemistry, Geophysics, Geosystems*, *13*(9). https://doi.org/10.1029/2012GC004162

Vannucchi, P., Remitti, F., & Bettelli, G. (2008). Geological record of fluid flow and seismogenesis along an erosive subducting plate boundary. *Nature*, *451*(7179), 699–703. https://doi.org/10.1038/nature06486

Venerdini, A., Alvarado, P., Ammirati, J.-B., Podesta, M., López, L., Fuentes, F., et al. (2020). Crustal seismicity in the Andean Precordillera of Argentina using seismic broadband data. *Tectonophysics*, *786*, 228450. https://doi.org/10.1016/j.tecto.2020.228450

Vilà, M., Fernández, M., & Jiménez-Munt, I. (2010). Radiogenic heat production variability of some common lithological groups and its significance to lithospheric thermal modeling. *Tectonophysics*, *490*(3–4), 152–164. https://doi.org/10.1016/j.tecto.2010.05.003

Wagner, L. S., Beck, S., & Zandt, G. (2005). Upper mantle structure in the south central Chilean subduction zone (30° to 36°S). *Journal of Geophysical Research: Solid Earth*, *110*(B1), B01308. https://doi.org/10.1029/2004JB003238

Wagner, L. S., Caddick, M. J., Kumar, A., Beck, S. L., & Long, M. D. (2020). Effects of oceanic crustal thickness on intermediate depth seismicity. *Frontiers of Earth Science*, *8*, 244. https://doi.org/10.3389/feart.2020.00244

Watts, A. B., & Burov, E. B. (2003). Lithospheric strength and its relationship to the elastic and seismogenic layer thickness. *Earth and Planetary Science Letters*, *213*(1), 113–131. https://doi.org/10.1016/S0012-821X(03)00289-9

Weiss, J. R., Qiu, Q., Barbot, S., Wright, T. J., Foster, J. H., Saunders, A., et al. (2019). Illuminating subduction zone rheological properties in the wake of a giant earthquake. *Science Advances*, *5*(12), eaax6720. https://doi.org/10.1126/sciadv.aax6720

Wessel, P., Luis, J. F., Uieda, L., Scharroo, R., Wobbe, F., Smith, W. H. F., & Tian, D. (2019). The generic mapping Tools version 6. *Geochemistry, Geophysics, Geosystems*, *20*(11), 5556–5564. https://doi.org/10.1029/2019GC008515

Wilks, K. R., & Carter, N. L. (1990). Rheology of some continental lower crustal rocks. *Tectonophysics*, *182*(1–2), 57–77. https://doi.org/10.1016/0040-1951(90)90342-6

Yáñez, G., & Cembrano, J. (2004). Role of viscous plate coupling in the late Tertiary Andean tectonics. *Journal of Geophysical Research: Solid Earth*, *109*(2). https://doi.org/10.1029/2003JB002494

Yáñez, G. A., Ranero, C. R., von Huene, R., & Díaz, J. (2001). Magnetic anomaly interpretation across the southern central Andes (32–34 S): The role of the Juan Fernández Ridge in the late Tertiary evolution of the margin. *Journal of Geophysical Research: Solid Earth*, *106*, 6325–6345. https://doi.org/10.1029/2000jb900337

References From the Supporting Information

Alvarado, P., Beck, S., & Zandt, G. (2007). Crustal structure of the south-central Andes Cordillera and backarc region from regional waveform modelling. *Geophysical Journal International*, *170*(2), 858–875. https://doi.org/10.1111/j.1365-246X.2007.03452.x

Alvarado, P., Pardo, M., Gilbert, H., Miranda, S., Anderson, M., Saez, M., & Beck, S. (2009). Flat-slab subduction and crustal models for the seismically active Sierras Pampeanas region of Argentina. In S. M. Kay, V. A. Ramos, & W. R. Dickinson (Eds.), *Backbone of the Americas: Shallow subduction, plateau uplift, and ridge and terrane collision*. Geological Society of America. https://doi.org/10.1130/2009.1204(12)

Ammirati, J.-B., Alvarado, P., & Beck, S. (2015). A lithospheric velocity model for the flat slab region of Argentina from joint inversion of Rayleigh wave phase velocity dispersion and teleseismic receiver functions. *Geophysical Journal International*, *202*(1), 224–241. https://doi.org/10.1093/gji/ggv140

Ammirati, J.-B., Venerdini, A., Alcacer, J. M., Alvarado, P., Miranda, S., & Gilbert, H. (2018). New insights on regional tectonics and basement composition beneath the eastern Sierras Pampeanas (Argentine back-arc region) from seismological and gravity data. *Tectonophysics*, *740–741*, 42–52. https://doi.org/10.1016/j.tecto.2018.05.015

Brocher, T. M. (2005). Empirical relations between elastic wavespeeds and density in the Earth's crust. *Bulletin of the Seismological Society of America*, *95*(6), 2081–2092. https://doi.org/10.1785/0120050077

Cacace, M., & Jacquey, A. B. (2017). Flexible parallel implicit modelling of coupled thermal–hydraulic–mechanical processes in fractured rocks. *Solid Earth*, *8*(5), 921–941. https://doi.org/10.5194/se-8-921-2017

Cammarano, F., Goes, S., Vacher, P., & Giardini, D. (2003). Inferring upper-mantle temperatures from seismic velocities. *Physics of the Earth and Planetary Interiors*, *138*(3), 197–222. https://doi.org/10.1016/S0031-9201(03)00156-0

Čermák, V., & Rybach, L. (1982). Thermal conductivity and specific heat of minerals and rocks. In G. Angenheister (Ed.), *Landolt-Börnstein: Numerical data and functional relationships in science and technology, new series, group V (Geophysics and space research), Volume ia. Physical properties of rocks)* (pp. 305–343). Springer.

Christensen, N. I., & Mooney, W. D. (1995). Seismic velocity structure and composition of the continental crust: A global view. *Journal of Geophysical Research: Solid Earth*, *100*(B6), 9761–9788. https://doi.org/10.1029/95JB00259

Conceição, R. V., Mallmann, G., Koester, E., Schilling, M., Bertotto, G. W., & Rodriguez-Vargas, A. (2005). Andean subduction-related mantle xenoliths: Isotopic evidence of Sr–Nd decoupling during metasomatism. *Lithos*, *82*(3–4), 273–287. https://doi.org/10.1016/j.lithos.2004.09.022

Gilbert, H., Beck, S., & Zandt, G. (2006). Lithospheric and upper mantle structure of central Chile and Argentina. *Geophysical Journal International*, *165*(1), 383–398. https://doi.org/10.1111/j.1365-246X.2006.02867.x

Goetze, C., & Evans, B. (1979). Stress and temperature in the bending lithosphere as constrained by experimental rock mechanics. *Geophysical Journal International*, *59*(3), 463–478. https://doi.org/10.1111/j.1365-246X.1979.tb02567.x

Götze, H.-J., & Lahmeyer, B. (1988). Application of three-dimensional interactive modeling in gravity and magnetics. *Geophysics*, *53*(8), 1096–1108. https://doi.org/10.1190/1.1442546

Hasterok, D., & Chapman, D. (2011). Heat production and geotherms for the continental lithosphere. *Earth and Planetary Science Letters*, *307*(1–2), 59–70. https://doi.org/10.1016/j.epsl.2011.04.034

He, L., Hu, S., Huang, S., Yang, W., Wang, J., Yuan, Y., & Yang, S. (2008). Heat flow study at the Chinese Continental Scientific Drilling site: Borehole temperature, thermal conductivity, and radiogenic heat production. *Journal of Geophysical Research*, *113*, B02404. https://doi.org/10.1029/2007JB004958

Jacquey, A. B., & Cacace, M. (2017). GOLEM, a MOOSE-based application (Version v1.0). *Zenodo*. https://doi.org/10.5281/zenodo.999401

Jalowitzki, T. L. R., Conceição, R. V., Orihashi, Y., Bertotto, G. W., Nakai, S., & Schilling, M. E. (2010). Evolução geoquímica de peridotitos e piroxenitos do Manto Litosférico Subcontinental do vulcão Agua Poca, Terreno Cuyania, Argentina. *Pesquisas em Geociencias*, *37*(2), 143. https://doi.org/10.22456/1807-9806.22656

Kennett, B. L. N., Engdahl, E. R., & Buland, R. (1995). Constraints on seismic velocities in the Earth from traveltimes. *Geophysical Journal International*, *122*(1), 108–124. https://doi.org/10.1111/j.1365-246X.1995.tb03540.x

Maaløe, S., & Aoki, K. (1977). The major element composition of the upper mantle estimated from the composition of lherzolites. *Contributions to Mineralogy and Petrology*, *63*(2), 161–173. https://doi.org/10.1007/BF00398777

McKenzie, D., Jackson, J., & Priestley, K. (2005). Thermal structure of oceanic and continental lithosphere. *Earth and Planetary Science Letters*, *233*(3–4), 337–349. https://doi.org/10.1016/j.epsl.2005.02.005

Ranalli, G., & Murphy, D. C. (1987). Rheological stratification of the lithosphere. *Tectonophysics*, *132*(4), 281–295. https://doi.org/10.1016/0040-1951(87)90348-9

Rodriguez Piceda, C., Scheck Wenderoth, M., Gomez Dacal, M. L., Bott, J., Prezzi, C. B., & Strecker, M. R. (2021). Lithospheric density structure of the southern Central Andes constrained by 3D data-integrative gravity modelling. *International Journal of Earth Sciences*, *110*(7), 2333–2359. https://doi.org/10.1007/s00531-020-01962-1

Schmidt, S., Götze, H.-J., Fichler, C., & Alvers, M. (2010). IGMAS+–a new 3D gravity, FTG and magnetic modeling software. In A. Zipf, K. Behncke, F. Hillen, & J. Scheffermeyer(Eds.), *GEO-INFORMATIK die welt im netz* (pp. 57–63). Akademische Verlagsgesellschaft AKA GmbH.

Sobolev, S. V., Zeyen, H., Stoll, G., Werling, F., Altherr, R., & Fuchs, K. (1996). Upper mantle temperatures from teleseismic tomography of French Massif Central including effects of composition, mineral reactions, anharmonicity, anelasticity and partial melt. *Earth and Planetary Science Letters*, *139*(1), 147–163. https://doi.org/10.1016/0012-821X(95)00238-8

Wiemer, S., & Wyss, M. (2000). Minimum magnitude of completeness in earthquake catalogs: Examples from Alaska, the Western United States, and Japan. *Bulletin of the Seismological Society of America*, *90*(4), 859–869. https://doi.org/10.1785/0119990114

Wyllie, P. (1981). Plate tectonics and magma Genesis. *Geologische Rundschau*, *70*(1), 128–153. https://doi.org/10.1007/BF01764318

Xu, Y., Shankland, T. J., Linhardt, S., Rubie, D. C., Langenhorst, F., & Klasinski, K. (2004). Thermal diffusivity and conductivity of olivine, wadsleyite and ringwoodite to 20 GPa and 1373 K. *Physics of the Earth and Planetary Interiors*, *143–144*, 321–336. https://doi.org/10.1016/j.pepi.2004.03.005